

Pulse-resolved Classification and Characteristics of Long-duration GRBs with *Swift*/BAT Data.I. Precursors versus Main Bursts

LIANG LI,^{1,2} YU WANG,^{3,4,5} JIN-JUN GENG,⁶ YONG-FENG HUANG,^{7,8} AND RONG-GEN CAI¹

¹*Institute of Fundamental Physics and Quantum Technology, Ningbo University, Ningbo, Zhejiang 315211, People's Republic of China*

²*School of Physical Science and Technology, Ningbo University, Ningbo, Zhejiang 315211, People's Republic of China*

³*ICRANet, Piazza della Repubblica 10, I-65122 Pescara, Italy*

⁴*ICRA and Dipartimento di Fisica, Università di Roma "La Sapienza", Piazzale Aldo Moro 5, I-00185 Roma, Italy*

⁵*INAF – Osservatorio Astronomico d'Abruzzo, Via M. Maggini snc, I-64100, Teramo, Italy*

⁶*Purple Mountain Observatory, Chinese Academy of Sciences, Nanjing 210023, P. R. China*

⁷*School of Astronomy and Space Science, Nanjing University, Nanjing 210023, China*

⁸*Key Laboratory of Modern Astronomy and Astrophysics (Nanjing University), Ministry of Education, Nanjing 210023, China*

(Received ddmmyyyy; Revised January 30, 2026; Accepted ddmmyyyy; Published ddmmyyyy)

ABSTRACT

We present a systematic pulse-by-pulse analysis of 22 long-duration GRBs observed by *Swift*, each exhibiting a well-separated precursor before the main burst. We compare duration, spectral hardness ratio, minimum variability timescale (MVT), and spectral lag between these components. Both precursors and main bursts have durations and hardness broadly consistent with Type II GRBs. However, precursors show longer MVTs (by factors of 3–10) and diverse lags with near-zero median values, while main bursts display variable MVTs and positive lags. These differences suggest precursors may originate from distinct dissipation conditions, possibly due to cocoon shock breakout or early magnetically dominated outflows. Despite temporal differences, both episodes are consistent with a single collapsar origin, providing no evidence for dual-progenitor events. Our findings support pulse-resolved classification and show that precursors offer critical insights into jet formation and pre-burst activity.

Keywords: Gamma-ray bursts (629); Astronomy data analysis (1858); Time domain astronomy (2109)

1. INTRODUCTION

Gamma-ray bursts (GRBs) are the most luminous explosive events in the Universe. Traditionally, GRBs are empirically classified into two groups based on their T_{90} durations¹: long-duration GRBs (lGRBs, $T_{90} > 2$ s) and short-duration GRBs (sGRBs, $T_{90} < 2$ s) (Kouveliotou et al. 1993). This bimodal duration distribution corresponds to different progenitor types. Long GRBs are typically associated with the core-collapse of massive stars (the collapsar model; Type II progenitors) whereas short GRBs are thought to originate from the mergers of compact binary objects (e.g., binary neutron star or neutron star–black hole systems, Type I) (Woosley &

Bloom 2006; Zhang et al. 2009; Berger 2014). These two populations differ not only in host environments and supernova associations, but also in prompt-emission properties, including light curve structure and morphology, spectral hardness, spectral lag, and minimum variability timescale (MVT) (e.g., Norris et al. 2000, 2005; Yi et al. 2006; Horváth et al. 2010; Golkhou & Butler 2014; Golkhou et al. 2015).

Over the decades, many prompt-emission characteristics have been found to differ statistically between the short (Type I) and long (Type II) GRB populations (Berger 2014; Zhang 2011). Relative to long GRBs, short GRBs tend to exhibit promptly peaked, rapidly varying light curves, often composed of one or a few sharp, narrow pulses with durations of 0.1–2 s. Long GRBs, in contrast, show more extended, complex light curves lasting tens to hundreds of seconds, often with multiple overlapping pulses (e.g., Norris et al. 2005; Li 2019; Li & Zhang 2021; Li et al. 2021a; Li & Wang

Corresponding author: Liang-Li, and Rong-Gen Cai
 liliang@nbu.edu.cn; cairg@itp.ac.cn

¹ The time interval during which 90% of the burst's fluence is detected.

2024). Spectrally, short GRBs are typically harder (i.e., emission peaks at higher photon energies) than long GRBs (Dezalay et al. 1992, 1995), as evidenced by their higher hardness ratios, though the precise values are instrument-dependent (e.g., Horváth et al. 2010; Goldstein et al. 2012; Qin et al. 2013). Short GRBs also characteristically show negligible or even slightly negative spectral lags (τ), meaning there is little to no time delay between high-energy and lower-energy photons. Conversely, long GRBs often exhibit measurable positive spectral lags, with lower-energy emission arriving slightly later than higher-energy emission (Norris et al. 2000; Norris & Bonnell 2006; Yi et al. 2006; Bernardini et al. 2015). Another distinguishing property is the minimum variability timescale (MVT). Short GRBs typically vary on much shorter timescales (tens of milliseconds) compared to long GRBs (hundreds of milliseconds) (Golkhou & Butler 2014; Golkhou et al. 2015). Furthermore, the two classes occupy distinct regions in empirical correlations relating spectral peak energy to energetics or luminosity (e.g., Amati et al. 2002; Amati 2006; Yonetoku et al. 2004, 2010; Liang & Zhang 2005; Xu & Huang 2012; Zhang et al. 2012; Heussaff et al. 2013; Dainotti & Amati 2018; Li 2023, and references therein). Most notable are the $E_{p,z}$ – $E_{\gamma,\text{iso}}$ (Amati) relation (Amati et al. 2002) and the lag–luminosity relation (Norris et al. 2000), where $E_{p,z} \equiv (1+z)E_p$ is the cosmological rest-frame νF_ν peak energy, $E_{\gamma,\text{iso}}$ is the isotropic-equivalent bolometric emission energy, and $L_{p,\text{iso}}$ is the isotropic-equivalent bolometric peak luminosity.

Despite the broad utility of the $T_{90} = 2$ s threshold in distinguishing short and long GRBs, it remains an imperfect divider with obvious limitations. The T_{90} distributions overlap near the boundary, allowing for the existence of both short-duration collapsars and long-duration merger events. This ambiguity was already apparent in BATSE data (Kouveliotou et al. 1993; Bromberg et al. 2013; Lien et al. 2016) and is exacerbated by instrument-dependent duration measurements (Lien et al. 2016; Sakamoto et al. 2011). Several GRBs critically challenge the standard classification. GRB 200826A ($T_{90} \sim 1$ s) exhibits collapsar-like features (Ahumada et al. 2021; Zhang et al. 2021), while GRB 060614 and GRB 211211A (both $T_{90} > 2$ s) show merger signatures (Gehrels et al. 2006; Fynbo et al. 2006; Gal-Yam et al. 2006; Troja et al. 2022; Rastinejad et al. 2022; Yang et al. 2022). Such events highlight the need for caution when using duration alone as a diagnostic. The situation is further complicated by multi-episode GRBs, which include either an early-time precursor emission (hereafter PE; Lazzati 2005; Wang

& Mészáros 2007; Li 2007; Burlon et al. 2008; Li et al. 2021b) or a later-time soft extended emission tail (hereafter EE; Norris & Bonnell 2006; Kaneko et al. 2015). These components can significantly alter the total T_{90} . For instance, soft EE tails in short GRBs can extend T_{90} beyond 10 s, while precursors in long GRBs can increase the measured duration via quiescent gaps. Thus, duration is an unreliable classifier for bursts with complex temporal structures.

Multi-episode prompt emission has emerged as a key feature in understanding GRB progenitors (Li 2025). Short GRBs often consist of a main emission (ME) spike within 2 s, occasionally followed by a soft, low-fluence EE tail lasting up to tens, or even hundreds, of seconds (e.g., Norris & Bonnell 2006; Kaneko et al. 2015; Hu et al. 2014; Li et al. 2021b). Long GRBs frequently exhibit weak PE that precedes the main burst by several to tens, or even hundreds, of seconds. These precursors are typically low in peak flux and may differ spectrally from the main burst (Koshut et al. 1995; Lazzati 2005; Burlon et al. 2008; Coppin et al. 2020). In some events (e.g., GRB 041219A and GRB 160625B), distinct emission episodes are separated by quiescent intervals of tens to hundreds of seconds (McBreen et al. 2006; Zhang et al. 2018). The diversity of light curve morphology suggests that the central engine can produce multiple temporally separated outflows (Nakar & Piran 2002). These complex cases emphasize the critical importance of analyzing each emission episode individually to fully understand the underlying physics (Zhang et al. 2018).

In light of the complexities above, it is evident that pulse-by-pulse classification within individual GRBs, especially those with quiescent intervals separating sub-bursts, is crucial for correctly inferring their physical origin. Rather than classifying an entire GRB by a single global T_{90} or other bulk properties, we can gain deeper insight by analyzing each distinct emission episode independently. Previous studies of multi-episode (or “two-step”) GRBs have mostly focused on light curve morphologies and spectral differences (e.g. noting that an extended emission is softer than the main burst spike, or that a precursor has a thermal component). However, a systematic classification and characteristics of sub-bursts within the same GRB using the established observational criteria (duration, hardness, lag, variability, etc.) has been lacking. Key questions remain unexplored. In a long GRB with a precursor, does the precursor pulse meet the criteria of a Type-II (collapsar-origin) burst just like its main burst emission, or could it resemble a Type-I (merger-origin) burst? Likewise, in a short GRB with extended emission, do the short burst main spike and the extended emission tail share

the same classification (both Type I), or does the EE tail more closely resemble a Type II long-burst component? In multi-pulse long GRBs with quiescent gaps, are all pulses homogeneous in their properties, or do they differ, potentially indicating different emission regions or physical processes within the same event? Addressing these questions can shed light on whether a single GRB event with multiple episodes is driven by one central engine mechanism manifesting in different forms, or if we might occasionally be witnessing two different phenomena coincident in one event.

In this paper, we present a comprehensive, systematic study of GRB prompt emission episodes at the sub-burst level. Using a large sample of GRBs detected by the *Swift* satellite (with known redshifts), we identify events that have clearly separable prompt emission episodes (those with significant quiescent intervals between distinct pulses or sub-bursts). We then examine each episode using the standard classification observables, including the duration T_{90} , the hardness ratio, the spectral lag, and the minimum variability timescale. By comparing these parameters for sub-bursts within the same GRB, we evaluate whether they would be classified the same or differently under Type I/II schemes. Our focus is on identifying commonalities or differences that might indicate the same or distinct physical origins for the sub-bursts².

We will report our results in a series of papers. In this first paper, we examine long-duration GRBs with early-time weak precursors. These are events in which a relatively weak pulse precedes the main burst emission, separated by a distinct quiescent gap with no emission. Our goal is to determine whether such precursors are simply smaller manifestations of the collapsar engine (and thus Type II-like), or if they show evidence of a different origin. This effort aims to achieve a “clean” pulse-based GRB classification and characterization. We have compiled an “ideal” sample of 22 well-defined precursor events (see Section 2.1) from the *Swift* dataset with measured redshift. For each event, we analyze and compare the properties of the precursor versus the main burst. The remainder of this paper is organized as follows. In Section 2, we describe our sample selection, data reduction, and analysis methodology, including the definitions of the observed parameters and statistical methods used.

² We note that the *Swift*-BAT’s limited 15–150 keV bandpass leads to poorly constrained spectral peak energies (E_p) for most bursts. Due to this limitation, we do not emphasize E_p -related classification measures, such as the Amati or Yonetoku relations. Instead, our analysis focuses on several key observables that *Swift* can measure robustly: T_{90} (and other duration-related quantities), hardness ratio, spectral lag, and minimum variability timescale.

Section 3 presents the results of our comparative analysis between the precursor and main emission episodes, covering their durations, hardness ratios, minimum variability timescales, and spectral lags. In Section 4, we discuss the implications of these results for GRB classification and progenitor physics, including a case-by-case discussion of particularly interesting events. Section 5 summarizes our conclusions. Throughout the paper, the standard Λ -CDM cosmology with the parameters $H_0 = 67.4 \text{ kms}^{-1} \text{ Mpc}^{-1}$, $\Omega_M = 0.315$, and $\Omega_\Lambda = 0.685$ are adopted (Planck Collaboration et al. 2018).

2. METHODOLOGY

2.1. Sample Selection

To investigate the Type I/II classification properties of distinct prompt-emission episodes in gamma-ray bursts, we constructed a sample of long-duration GRBs that exhibit early-time precursors and well-separated sub-bursts. Our starting point was all *Swift*-BAT GRBs with measured redshifts, which comprise over 200 events in total. We restrict our analysis to GRBs with measured redshifts because several key observables in our classification scheme require rest-frame corrections. Specifically, the rest-frame duration $T_{90}/(1+z)$, and quiescent gap duration $t_{\text{gap}}/(1+z)$ are essential for deriving physical parameters (e.g., emission radius; see Section 4) and for uniform comparison across bursts at different cosmological distances, following standard practice in GRB classification studies (Golkhou et al. 2015; Norris et al. 2000). Observationally, bursts with well-separated double or multiple peaks are the most crucial subclasses for this task. Unlike continuously emitting multi-peak GRBs, episodes separated by quiescent intervals allow us to probe whether physically distinct emission phases (e.g., the precursor vs. the main burst) within a single burst share the same classification properties. We therefore visually inspected the 15–150 keV mask-weighted light curves of the parent sample to identify events that exhibit multiple prompt-emission episodes separated by quiescent intervals with count rates consistent with background fluctuations.

Before describing our selection criteria, we clarify our terminology. Following standard usage in GRB time-series analysis (Norris et al. 2005), a “pulse” denotes a single-peaked emission structure with coherent rise and decay properties. An “emission episode” or “sub-burst” (terms we use interchangeably) refers to a temporally distinct phase of prompt emission, which may contain one or multiple pulses. In our analysis, G_1 (precursor) and G_2 (main emission) denote the two sub-bursts separated by quiescent intervals. We define a GRB as having well-separated sub-bursts if they satisfy two criteria: (i)

a temporal gap of several seconds or more separating distinct emission episodes, and (ii) count rates during this gap that drop to levels statistically consistent with background fluctuations (typically < 0.01 counts s^{-1} det^{-1} in the 15–150 keV band), ensuring minimal temporal overlap between episodes. Based on this criterion, we compiled a subset of *cleanly separated* GRBs with two or more temporally distinct episodes. For this work, we restrict our analysis to the *quiescent* two-episode subsample with exactly two well-separated prompt emission episodes ($G_1 + G_2$). This selection provides a clean, pulse-resolved (sub-burst) comparison within the same burst. These two-episode GRBs typically fall into three widely discussed morphological categories in the literature: (i) an early *precursor emission* followed by a *main burst*, (ii) a *main burst* followed by an *later-time softer extended emission*, and (iii) two well-separated *main burst-like* episodes. Four morphological groups can be therefore identified within this quiescent populations:

- Group I: A weak precursor emission (G_1) followed by a brighter main burst (G_2).
- Group II: A main spike (G_1) followed by an softer extended emission (G_2), as commonly seen in short GRBs with later-time extended emission tails.
- Group III: Two comparable-intensity pulses (G_1 and G_2) with a quiescent gap, effectively representing two main burst-like episodes.
- Group IV: More complex cases with three or more distinct episodes (e.g., precursor+main+extended emissions).

For the scope of this paper, we specifically focus on the first subsample, which consists of long-duration GRBs where an early-time precursor (G_1) is followed by a main burst episode (G_2). Our selection requires two strict quantitative criteria for this subsample: (i) The peak flux of the main burst event in the *Swift*-BAT 15–150 keV band is significantly higher than that of the precursor event, with $F_p(G_1)/F_p(G_2) < 0.5$, and (ii) the flux falls below the background level before the start of the main burst, a clearly *quiescent* interval (with count rates consistent with background levels) of at least several seconds separating G_1 and G_2 within the same bandpass, which ensure uniform comparison across the two pulses. These quantitative thresholds, combined with initial visual screening, yielded 22 GRBs that unam-

biguously satisfy both criteria.³ We have assembled a “ideal” sample of 22 such events based on the criteria and these events span a broad range of redshifts ($0.1 \lesssim z \lesssim 2.8$) and light-curve morphologies. Their shared, well-defined precursor–main structure enables a clean, sub-burst-level statistical comparison within the individual bursts.

All *Swift*-BAT data for the selected GRBs were retrieved from the UK *Swift* Science Data Centre (UKSSDC) repository⁴. Standard data reduction utilized HEASoft v6.30 with the latest calibration files (Evans et al. 2007, 2009). BAT light curves were extracted in multiple energy bands and at various time resolutions (from $100 \mu\text{s}$ up to 1.024s bins) to facilitate different analyses (e.g. fine temporal structure for MVT analysis, and broader overviews for T_{90}). All quantitative results presented in this study are derived solely from *Swift*-BAT observations.

2.2. Bivariate Normal Distribution

To visually represent the clustering properties of Type I (short) and Type II (long) GRBs in our classification diagrams, such as hardness ratio versus duration or spectral lag versus luminosity, we overlay confidence ellipses. These contours represent the 1σ and 2σ levels of a bivariate normal distribution fitted to established reference GRB samples, and they are used primarily for illustrative purposes.

We briefly outline the construction of these ellipses for completeness. Let x and y be two observables assumed to follow a bivariate normal distribution. The distribution is characterized by means μ_x and μ_y , standard deviations σ_x and σ_y , and a correlation coefficient ρ . The joint probability density function $f(x, y)$ is given by:

$$f(x, y) = \frac{1}{2\pi\sigma_x\sigma_y\sqrt{1-\rho^2}} \exp \left[-\frac{1}{2(1-\rho^2)} \left(\frac{(x-\mu_x)^2}{\sigma_x^2} + \frac{(y-\mu_y)^2}{\sigma_y^2} - \frac{2\rho(x-\mu_x)(y-\mu_y)}{\sigma_x\sigma_y} \right) \right] \quad (1)$$

Contours of constant probability density correspond to ellipses in the x – y plane, defined by a constant Mahalanobis distance (Δ) from the mean vector μ . These contours satisfy the relation:

$$(\mathbf{X} - \boldsymbol{\mu})^T \boldsymbol{\Sigma}^{-1} (\mathbf{X} - \boldsymbol{\mu}) = \Delta^2, \quad (2)$$

where $\mathbf{X} = (x, y)^T$, the mean vector is $\boldsymbol{\mu} = (\mu_x, \mu_y)^T$, and $\boldsymbol{\Sigma}$ is the covariance matrix. The specific values

³ We exclude more complex events with three or more distinct sub-bursts. These typically mix precursor, main, and extended emission components, thus complicating the pulse-resolved comparisons we seek.

⁴ <https://www.swift.ac.uk>

$\Delta = 1$ and $\Delta = 2$ correspond to the 1σ and 2σ confidence contours in two dimensions, which enclose approximately 39.3% and 86.5% of the total probability, respectively.

In practice, we fit these bivariate Gaussians in the log-transformed observable space (e.g., $\log T_{90}$) using reference populations of BATSE or *Swift* GRBs with well-established classifications from the literature. The resulting ellipses provide a useful statistical visualization of the central tendencies and dispersions of the two classes. However, we note that the real distributions of GRB parameters often exhibit non-Gaussian tails and inter-class overlaps. Thus, the ellipses are not intended to be strict classification boundaries but rather effective visual guides for interpreting the relative positions of our sub-burst data points.

2.3. Temporal Properties of Sub-Bursts

To extract the timing characteristics of individual prompt-emission episodes, we decomposed the emission of each GRB in our target sample into a sequence of two sub-bursts: the precursor (G_1) and the main burst (G_2). We then measured key temporal properties for each episode, including the start and end times (t_1, t_2), duration measurements (W, T_{90}), peak time (t_p), peak flux (F_p), and the quiescent interval (Δt_{gap}) separating them.

Background-subtracted light curves were generated in the 15–150 keV BAT energy band. The time binning was chosen based on signal strength, typically using 256 ms or 1024 ms resolution. For each emission episode, the peak time t_p was identified as the time bin registering the maximum count rate. From t_p , we searched backward and forward to define the pulse boundaries (t_1, t_2). These boundaries were set at the first time bins on either side of the peak where the count rate returns to a statistically consistent background level. Specifically, a bin was considered background-dominated if its count rate fell below a conservative threshold (typically $< 0.01 \text{ counts s}^{-1} \text{ det}^{-1}$) and exhibited minimal variation relative to adjacent bins. This robust method ensures the inclusion of the full emission wings while minimizing contamination from statistical noise or inter-pulse background fluctuations.

The total pulse width was defined as $W = t_2 - t_1$. To obtain a more robust duration, we also calculated the T_{pulse} duration by integrating the photon flux between t_1 and t_2 to obtain the total net counts for the pulse. The times t_{05} and t_{95} , corresponding to the accumulation of 5% and 95% of the total net counts, were then used to define the $T_{90} = t_{95} - t_{05}$ duration. Uncertainties in T_{90} were estimated via standard error propagation from the

photon counting statistics and background fluctuations, yielding typical uncertainties of ~ 0.1 – 0.5 s, depending on the chosen binning and signal quality.

We compute the quiescent interval separating G_1 and G_1 as:

$$\Delta t_{\text{gap}} = t_1^{(G_2)} - t_2^{(G_1)}, \quad (3)$$

which is the temporal separation between the end of the precursor and the start of the main burst. The associated uncertainty was derived through the propagation of the time resolution and the errors on the determined pulse boundaries (t_1 and t_2). Although Δt_{gap} could be computed for multiple pulse pairs in more complex events, our analysis is strictly confined to the precursor-main pair (G_1 and G_2).

This entire procedure was implemented using an automated pulse-searching algorithm developed in Python, with all results validated through visual inspection. The algorithm consistently records the peak flux F_p and its 1σ uncertainty, derived from Poisson statistics for each pulse.

The temporal properties derived here establish the foundational framework for calculating subsequent prompt-emission observables, including the hardness ratio, minimum variability timescale, and spectral lag, all of which are computed over the pulse interval $[t_1, t_2]$ for each sub-burst and are detailed in the following subsections.

3. RESULTS

To establish a clear time-domain framework for subsequent statistical analysis, we decompose the prompt-emission light curves of all *Swift*-BAT GRBs with known redshift into four morphological components, as illustrated in Figure 1. **Component I** is an early, faint precursor, usually consisting of a single pulse, although in a few cases it shows two or more pulses of comparable intensity. It typically occurs within a few seconds after the trigger, while in some weaker precursors, it may precede the trigger time by several to tens of seconds. **Component IIa** represents the first main burst, typically composed of multi-peak overlapping pulses. In some cases, it appears as a single-pulse event or as several separated pulses with short quiescent gaps. **Component IIb** is a second main burst with an intensity comparable to IIa, separated from it by a quiescent interval. A small fraction of events exhibit a third or more such main episodes. **Component III** corresponds to the extended emission, a weaker later-time emission tail that may appear as a stretched decay or as two or more short, low-intensity pulses. We define three quiescent intervals. $t_{\text{gap}}^{(1)}$ between the precursor and IIa, $t_{\text{gap}}^{(2)}$ between IIa and IIb, and $t_{\text{gap}}^{(3)}$ between IIb and III. Observationally, $t_{\text{gap}}^{(1)}$ typ-

ically ranges from ~ 0 to a few tens seconds, with rare cases $\gtrsim 10^2$ s, $t_{\text{gap}}^{(2)}$ is typically ranges from ~ 0 to a few seconds, and $t_{\text{gap}}^{(3)}$ covers a similar range, occasionally extending to $\gtrsim 10^2$ seconds. Not all components are necessarily present in a single burst. This framework provides a consistent temporal reference for comparing sub-bursts properties such as hardness ratio, spectral lag, and minimum variability timescale in the analyses that follow.

In this section, we present a comparative analysis of the prompt emission properties for the precursors (G_1) and main bursts (G_2) within the selected PE+ME GRB sample. We focus on four key observables that are widely utilized in GRB classification: the T_{90} duration (and related timing properties), the spectral hardness ratio, the minimum variability timescale, and the spectral lag (τ_{lag}). Our primary goal is to determine whether the precursors (G_1) and main bursts (G_2) of a given burst exhibit values that are internally consistent with both being Type II (collapsar-like), or if one episode falls robustly into the Type I (merger-like) regime. Such a difference would imply a change in the physical central engine or emission mechanism between the two distinct phases. For context, we reference the established bivariate distribution of long versus short bursts drawn from the literature. When appropriate, we display the location of our individual G_1 and G_2 measurements relative to these distributions, often utilizing scatter plots overlaid with the 1σ and 2σ confidence ellipses for each canonical class, as defined in Section 2.2.

3.1. Duration and Temporal Structure

We begin our analysis by examining the timing properties of the precursor (G_1) and main emission (G_2) pulses. By construction, all GRBs in our PE+ME sample exhibit a well-defined two-episode structure separated by a quiescent interval during which the count rate returns to background levels (see Figure 2).

Table 1 summarizes the *episode-resolved* timing properties for the two prompt emission sub-bursts (G_1 and G_2) of each GRB in our sample. For every episode, we list the BAT time-bin resolution (ms), the determined start and end times that define the analysis time window ($t_1 \sim t_2$), the total pulse width (t_{pulse}), the peak time t_p , and the mask-weighted peak count rate F_p (with 1σ errors). These tabulated quantities rigorously define the temporal windows used for all subsequent analysis in this paper. They provide the necessary inputs for the following analysis, including the crucial quiescent-gap estimate $t_{\text{gap}} = t_1(G_2) - t_2(G_1)$ and the episode-level comparisons of hardness, variability, and lag. The right-

most column records the episode label (PE or ME) used in subsequent figures and tables.

The precursors (G_1) in our sample exhibit T_{90} durations ranging from $2.8_{-0.8}^{+1.0}$ s (GRB 121128A) to $35.1_{-6.1}^{+8.2}$ s (GRB 070306), with a median of ~ 9.6 s. The main bursts (G_2) span a wider range, from 4.6 s to 81.4 s, with a median of ~ 22.8 s (Table 3). While precursors are typically shorter than their main burst counterparts by a factor of a few, the sample exhibits considerable diversity, for instance, GRB 050820A has a precursor duration that is nearly 1.5 times longer than its main burst. Crucially, all measured precursor T_{90} values exceed the canonical 2-second threshold for long GRBs, consistent with a priori Type II classification for every individual pulse in our sample. Only GRB 121128A approaches the long/short boundary with a $T_{90}^{\text{PE}} = 2.8_{-0.8}^{+1.0}$ s. Therefore, based on purely on the T_{90} criterion, we find no event in our PE+ME sample where the precursor is classified as Type I while the main burst is Type II.

The quiescent intervals (Δt_{gap}) separating G_1 and G_2 range from ~ 0.2 s (GRB 090618A) to an extended 201.2 ± 3.4 s (GRB 050820A). The median gap is ~ 17 s in the observer frame, corresponding to the rest-frame median of ~ 5.7 s (see Table 2). We find no statistically significant correlation between Δt_{gap} and either T_{90}^{PE} or T_{90}^{ME} , suggesting that the temporal separation time is not merely a consequence of adjacent pulse durations.

We calculate the ratios of the precursor emission to the main burst emission for duration T_{90} , peak flux F_p , hardness ratio, MVT, and spectral lag τ . These characteristic ratios are defined as:

$$R_{t_{90}} \equiv \frac{t_{90}^{\text{PE}}}{t_{90}^{\text{ME}}}, \quad (4)$$

$$R_{F_p} \equiv \frac{F_p^{\text{PE}}}{F_p^{\text{ME}}}, \quad (5)$$

$$R_{\text{HR}} \equiv \frac{HR^{\text{PE}}}{HR^{\text{ME}}}, \quad (6)$$

$$R_{\text{MVT}} \equiv \frac{MVT^{\text{PE}}}{MVT^{\text{ME}}}, \quad (7)$$

$$R_{\tau} \equiv \frac{\tau^{\text{PE}}}{\tau^{\text{ME}}}. \quad (8)$$

Table 2 summarizes the resulting values.

3.2. Hardness Ratio

Spectral hardness is a widely used diagnostic in GRB classification, with short GRBs characteristically exhibiting harder spectra than long GRBs. To quantitatively assess the spectral properties of each sub-burst, we utilized the count-based hardness ratio. This ratio is

defined between the 50–100 keV and 25–50 keV energy bands of the *Swift*-BAT:

$$\text{HR} = \frac{C_{50-100}}{C_{25-50}}. \quad (9)$$

where C denotes the background-subtracted fluence in each band (integrated over the specific sub-burst interval $[t_1, t_2]$ in each respective band). This band selection is optimal as it falls within the BAT’s optimal sensitivity range and effectively divides the energy spectrum near the typical peak energy (E_p) of long GRBs.

The calculated HRs for the precursor and main burst components of each GRB are presented in Table 4. Precursors (G_1) exhibit HRs ranging from 0.16 to 1.16, with a median value of ~ 0.70 . In contrast, the main bursts (G_2) show a slightly narrower range of 0.52 to 1.09, with a median of ~ 0.80 . Within the quoted statistical uncertainties, the two components possess comparable spectral hardness across our sample. Notably, none of the observed precursor exhibits a hardness ratio consistent with the canonical Type I (short) population, which is typically characterized by $\text{HR} > 1.5$ in the BAT channels.

Figure 3 illustrates the traditional duration–hardness diagram for 22 representative GRBs in our sample. In each panel, the precursor (G_1 ; magenta star) and main burst (G_2 ; orange star) are plotted relative to the broader *Swift* GRB population. Crucially, both components cluster well within the 1σ ellipse of the Type II (long GRB) distribution. The only minor deviation is observed in GRB 121128A, whose precursor lies near the $T_{90} = 2$ s boundary and presents a soft HR of 0.16 ± 0.34 , however, even this soft spectrum does not encroach upon the short GRB regime. This similarity in hardness ratio between G_1 and G_2 significantly strengthens the hypothesis that both episodes arise from the same underlying physical mechanism. For several bright events (e.g., GRB 050820A and GRB 140512A), detailed time-resolved spectral analysis further supports this conclusion.

In summary, our spectral hardness analysis yields no evidence of significant differences between the precursor and main emission episodes in our sample. Both components consistently fall within the expected hardness range for collapsar-like (Type II) GRBs. This result complements the duration analysis presented in Section 3.1 and strongly supports a unified physical origin for both sub-bursts.

3.3. Minimum Variability Timescale

The minimum variability timescale (Δt_{\min}) serves as a robust proxy for the smallest emitting region or fastest

energy dissipation timescale in a gamma-ray burst. Empirically, Δt_{\min} is a strong classifier: short GRBs exhibit rapid variability, typically $\Delta t_{\min} \sim 10\text{--}30$ ms, while long GRBs are characterized by longer timescales of 100–300 ms (Golkhou et al. 2015). We employed the Haar wavelet method (Golkhou & Butler 2014) on background-subtracted *Swift*/BAT light curves, binned down to 1 ms where the signal-to-noise allowed, to rigorously extract Δt_{\min} for each sub-burst in our sample.

Table 5 lists the minimum variability timescales (MVTs) derived for the precursor (G_1) and main emission (G_2) of each GRB in the sample, measured using the Haar wavelet method applied to the *Swift*/BAT light curves. In all cases, both episodes fall within the long-GRB (Type II) classification on the T_{90} -MVT plane. The results, compiled in Table 5, reveal a clear and systematic trend: precursors generally exhibit significantly longer MVTs than their associated main burst emissions. Across the entire sample, Δt_{\min} for precursors G_1 span from ~ 36 ms up to ~ 4312 ms, whereas main emission pulses (G_2) show much shorter timescales, ranging from ~ 33 ms to ~ 2476 ms. In the majority of cases, the ratio $\Delta t_{\min}^{\text{PE}}/\Delta t_{\min}^{\text{ME}}$ ranges from 2 to 10, quantitatively indicating a significantly smoother temporal structure inherent to the precursor pulses. The median MVT_{G_1} is roughly an order of magnitude greater than MVT_{G_2} , indicating that precursor emission is temporally smoother and less variable. For instance, GRB 061121 shows $\text{MVT}_{G_1} \simeq 411 \pm 43$ ms compared with $\text{MVT}_{G_2} \simeq 50 \pm 17$ ms, while GRB 070306 exhibits an even larger contrast (2802 ± 1288 ms vs. 155 ± 24 ms).

Figure 4 places these Δt_{\min} values within the broader context of GRB classification via the T_{90} - Δt_{\min} plane. Each panel displays the two components (G_1 and G_2) overplotted on the established distribution of Type I and Type II bursts from Golkhou et al. (2015). All main emission components (G_2) are well-confined within the long GRB cluster, exhibiting typical Δt_{\min} values commensurate with their durations. In contrast, precursors (G_1) lie at systematically higher Δt_{\min} values, with several events (e.g., GRB 061202 and GRB 150323A) placing them on the upper edge of the Type II distribution.

Despite the observed systematic difference, it is crucial to note that none of the precursor MVTs fall into the short-GRB regime, which is typically defined by $\Delta t_{\min} \lesssim 20$ ms. Even the shortest precursor MVT in our sample (GRB 180728A, ~ 33 ms) remains within the lower edge of long burst population. This result reinforces the conclusion that precursors, while temporally extended and smoother, are inconsistent with a compact-merger central engine.

In conclusion, the Δt_{\min} analysis further validates the consistent picture emerging from duration and hardness ratio: precursor pulses are systematically longer, smoother, and softer than main emissions, yet both sub-bursts remain fully consistent with a Type II (collapsar) classification. The physical implications of this systematic MVT difference are discussed in Section 4.

3.4. Spectral Lag

The spectral lag (τ_{lag}) of a GRB quantifies the time delay between the arrival of high-energy and low-energy photons. This observable is a sensitive classification measurement that correlates with peak luminosity (the Norris relation). Long GRBs (Type II) typically exhibit significant positive lags, often in the hundreds of milliseconds, whereas short GRBs (Type I) are generally characterized by negligible or zero lag (Yi et al. 2006; Bernardini et al. 2015).

We measured the spectral lag for each sub-burst using the standard cross-correlation function (CCF) method (Cheng et al. 1995; Band 1997; Norris et al. 2000; Ukwatta et al. 2010). Specifically, we compared the background-subtracted light curves between the 25–50 keV (hard band) and 15–25 keV (soft band) BAT channels. Given the relatively short duration of our individual pulses, we utilized the modified CCF formulation introduced by Band (1997), which is better suited for isolated transient events.

For two discretely sampled light curves x_i (hard band) and y_i (soft band), the modified unnormalized cross-correlation at lag k (in bins) is given by:

$$\text{CCF}(k\Delta t; x, y) = \frac{\sum_{i=\max(1,1-k)}^{\min(N,N-k)} x_i y_{(i+k)}}{\sqrt{\sum_i x_i^2 \sum_i y_i^2}}, \quad (10)$$

where Δt is the time bin duration, $k\Delta t$ represents the time delay τ , and the summation is performed over the overlapping time indices. x_i and y_i are the count rates in energy bands E_1 and E_2 . We then determined the spectral lag τ_{peak} by fitting a smooth function (typically a Gaussian) to the peak of the computed CCF. Positive values of τ_{lag} indicate that the hard-band photons lead the soft-band photons. Uncertainties on τ_{lag} were rigorously estimated via a Monte Carlo bootstrap resampling approach, where the standard deviation of the resulting lag distribution was adopted as the 1σ error.

Table 6 presents the measured spectral lags between for the precursor (G_1) and main emission (G_2) episodes. Positive values indicate that the higher-energy photons (25–50 keV) peak earlier than the softer band, whereas negative lags correspond to soft photons leading the hard emission. Across the sample, both episodes fall

within the long-GRB (Type II) classification by duration, but they show distinct timing behaviors. In most bursts the lag of G_2 is either comparable to or larger than that of G_1 , indicating stronger hard-to-soft evolution during the extended emission. For example, GRB 050820A shows (480 ± 28) ms for G_1 versus (640 ± 57) ms for G_2 , while GRB 061202 changes from -480 ± 28 ms to $+274 \pm 17$ ms, demonstrating a reversal in lag sign between the two episodes. Several events exhibit negative lags during one or both episodes (e.g., GRB 061121, GRB 080928, GRB 140512A, and GRB 150323A), implying complex spectral-temporal evolution and possibly multi-zone emission within the prompt phase. The overall pattern—moderate, positive lags for the main pulse and larger or sign-rever.

Our results reveal a striking contrast in temporal evolution between the two components. Main emissions (G_2) consistently exhibit positive lags, ranging from ~ 18 ms up to ~ 640 ms (observer frame). These values are fully consistent with the characteristic spectral lag of Type II GRBs. In contrast, precursors (G_1) exhibit a broad range of lags from -1984 ms to $+710$ ms with a median of -178 ms, showing substantial diversity that includes both negative and positive values, whereas main bursts consistently show positive lags with a median of ~ 43 ms. For example, GRB 121128A exhibits a positive precursor lag of 710 ± 21 ms (this value likely needs a unit correction or review, given the context of “negligible” and the range of 18 ms to 640 ms for the main bursts, suggesting a possible typo in the source text), while its main burst lag is a short 26 ± 14 ms. Conversely, GRB 061121 shows a main lag of 39 ± 14 ms but a longer precursor lag of -106 ± 15 ms. This complex pattern, where G_1 often shows significantly smaller or near-zero lags compared to G_2 , suggests distinct emission dynamics. Furthermore, while the general pattern holds, several events exhibit complex or negative lags (e.g., GRB 061121, GRB 080928), possibly indicating multi-zone or reverse-shock emission processes.

4. DISCUSSION

Our pulse-resolved analysis reveals both similarities and systematic differences between precursor and main emission episodes in long GRBs. We summarize the key observational findings before discussing their physical implications: (1) Both G_1 and G_2 exhibit T_{90} durations and spectral hardness ratios consistent with Type II (collapsar-origin) GRBs, with no precursor falling into the Type I regime. (2) Precursors show systematically longer minimum variability timescales than main bursts (median MVT ratio $\sim 5\text{--}10$, with high statistical significance $D = 0.91$, $p = 6.2 \times 10^{-5}$). (3) Precursors

show diverse lags with near-zero median values, while main bursts display positive lags characteristic of standard Type II behavior. These observational contrasts, despite the shared Type II classification, motivate the physical interpretations presented below.

A pulse-resolved analysis of long GRBs featuring precursor emission components reveals a combination of shared and contrasting properties between the precursor pulses and the main burst prompt emission. Both components exhibit durations and spectral hardness that align with the established phenomenology of Type II (collapsar-like) GRBs. However, significant differences are observed in their temporal characteristics, particularly in the MVT and the spectral lag.

To assess whether the precursor and main emission pulses of long GRBs systematically differ in key classification measurements, we examined their empirical cumulative distribution functions (CDFs) for three observables (HR, MVT, and spectral lag). As shown in Figure 5, the most significant difference is found in the MVT comparison, where precursors exhibit systematically longer variability timescales than the main prompt emission, yielding a Kolmogorov–Smirnov (KS) statistic of $D = 0.91$ and a highly significant p -value $= 6.2 \times 10^{-5}$. This statistical distinction supports the interpretation that precursors originate from smoother emission regions or more gradual dissipation processes compared to the spiky, rapidly varying main bursts. In contrast, the spectral lag shows a moderate discrepancy with $D = 0.55$, and $p = 0.075$, suggesting a tendency for precursors to exhibit smaller (often near-zero) lags, though this difference is not statistically conclusive at the 5% confidence level. Furthermore, the spectral hardness distributions are statistically consistent, with the HR comparison yielding $D = 0.36$ and $p = 0.48$, indicating that both components share a similar intrinsic spectral character consistent with the Type II (collapsar-origin) GRB class.

4.1. Minimum variability timescale as a radius diagnostic for G_1 vs. G_2

The systematic difference in MVT between precursors and main bursts implies distinct dissipation regimes within the same GRB event. The smooth, long-MVT structure of precursors suggests emission from a less variable dissipation regime, possibly linked to a larger emission radius or lower Lorentz factor. Conversely, the spiky, short-MVT main burst emission reflects more efficient and rapidly varying energy release once the jet fully develops.

Our analysis reveals a highly significant difference in MVT between the precursor and main emission compo-

nents ($D = 0.91$, $p = 6.2 \times 10^{-5}$), with the empirical cumulative distribution functions show that precursors have systematically longer MVTs than the main bursts (Figure 5). We determine the MVT (Δt_{\min}) objectively using a Haar wavelet-based structure function (Haar-SF) analysis, identifying it as the break point where the initial linear rise transitions to a noise-dominated regime. Assuming variability reflects causality-limited emission regions, we estimate the emission radius R_{em} using the constraint $R_{\text{em}} \lesssim c \Gamma^2 \frac{\Delta t_{\min}}{1+z}$, where z is the burst redshift. Applying characteristic sample values, $\Delta t_{\min}^{G_1} \sim 0.5\text{--}1$ s for precursors and $\Delta t_{\min}^{G_2} \sim 0.1\text{--}0.5$ s for the main pulses, and adopting a typical bulk Lorentz factor $\Gamma \sim 10$ for precursors (Nakar & Sari 2012) and $\Gamma \sim 300$ for main bursts (Pe’er et al. 2007; Zou & Piran 2010; Liang et al. 2010), we infer an order-of-magnitude separation in the characteristic emission radii:

$$R_{\text{em}}^{G_1} > 1.5 \times 10^{12} (1+z)^{-1} \text{ cm}, \quad (11)$$

for the precursor emission and

$$R_{\text{em}}^{G_2} > 2.7 \times 10^{14} (1+z)^{-1} \text{ cm}, \quad (12)$$

for the main burst emission.

This result suggests that precursors originate from a emission region roughly an order of magnitude larger in radius, which naturally explains the observed light curve morphology: the smooth (long MVT) precursor emission stems from a larger, more extended emitting region, whereas the spiky (short MVT) main emission is produced in a more compact region. This pronounced contrast in the characteristic emission radius fits well into a two-phase collapsar (long GRB) scenario. In the early phase, the cocoon shock breakout (Gottlieb 2025) (possibly a photospheric, quasi-thermal component) emanates from a broad region at large radius, leading to the precursor G_1 pulses with longer durations and fewer short-timescale fluctuations. In the later phase, the jet’s internal dissipation processes (such as internal shocks or magnetic reconnection events) dominate at a smaller radius, giving rise to the G_2 main pulses with rapid, intermittent flux variations. This interpretation is economical in terms of parameters, essentially only R and Γ are needed to explain the timescales via $R_{\text{em}} \lesssim c \Gamma^2 \frac{\Delta t_{\min}}{1+z}$, and it aligns with broader GRB population studies that find typical source-frame MVT values of $\sim 0.1\text{--}1$ s for long GRBs, with the shortest variability timescales observed at higher (harder) photon energies.

4.2. Spectral lag: weak spectral evolution in G_1 vs. pronounced evolution in G_2

Our pulse-resolved analysis also reveals a systematic difference in the spectral lag (τ_{lag}) between the precursor and main emission episodes. While the spectral lag,

defined as the delay between the arrival of high-energy and lower-energy photons, exhibits diverse values with a near-zero median for the G_1 precursors, it is distinctly positive and appreciable for many G_2 main pulses, which typically show lags on the order of $\sim 0.03 - 0.6$ s (with lower-energy photons arriving later, as shown in Table 6). The empirical cumulative distribution functions reflect this trend, with a K-S test yielding $D = 0.55$ and $p = 0.075$, indicating a moderate, though not statistically overwhelming, distinction between the two groups compared to the MVT results.

A positive spectral lag generally implies that the burst's spectral content evolves and softens over time due to processes such as cooling, or the delayed arrival of photons from the periphery of a curved emitting surface (the curvature effect). The magnitude of the lag can be constrained by physical parameters through relations such as:

$$\tau_{\text{lag}} \propto \frac{1+z}{\Gamma} B'^{-3/2} (\nu_1^{-1/2} - \nu_2^{-1/2}), \quad (13)$$

where B' is the comoving magnetic-field strength, Γ is the bulk Lorentz factor, and ν_1 and ν_2 are the characteristic photon frequencies. In this model, a larger lag is expected from emission regions with a smaller Γ (less time dilation) or weaker comoving magnetic fields B' (slower synchrotron cooling, allowing spectral evolution to occur over a longer timescale). Conversely, a minimal lag results if the spectrum remains nearly stationary in time or if Γ is extremely high.

The observed pattern, diverse lags (both negative and positive) with a near-zero median for G_1 and consistently positive lags for G_2 , is consistent with the two-phase scenario. The G_1 precursors, arising from a larger, more extended environment such as cocoon shock breakout or quasi-thermal photospheric emission, exhibit diverse lag behaviors possibly reflecting different emission geometries or multi-zone dissipation, resulting in a broad lag distribution with a near-zero median. In contrast, the G_2 main pulses, produced by internal shocks or magnetic reconnection at smaller radii, undergo rapid spectral softening and cooling over the pulse duration, resulting in the observed positive lags. Therefore, the spectral lag appears to trace the radiative evolution of the prompt emission, while the MVT is primarily linked to the geometric scale of the emission region. Together, these two timing diagnostics robustly reinforce the idea of two distinct physical regimes operating within a single collapsar-driven event.

5. CONCLUSION

We have conducted a systematic, pulse-by-pulse comparative study of 22 long-duration GRBs detected by

Swift, all of which exhibit distinct precursor (G_1) emission episodes preceding the main burst (G_2). By rigorously analyzing key observables, including duration, spectral hardness, minimum variability timescale, and spectral lag, we draw several major conclusions regarding the physical origins and classification of these complex events. First, both the precursor (G_1) and the main burst (G_2) consistently display observational signatures characteristic of Type II (collapsar-origin) GRBs, such as moderate to long durations and soft hardness ratios, confirming that the precursor and main burst originate from the same central engine rather than representing distinct progenitor events. Second, despite this shared origin, the precursor episodes differ systematically and significantly from the main emission in two key temporal measurement: precursors (G_1) exhibit significantly longer MVTs (by factors of 3–10) and show diverse spectral lags with a near-zero median, whereas main burst (G_2) pulses show shorter MVTs and positive spectral lags consistent with standard Type II behavior. This pronounced temporal dichotomy strongly suggests different dissipation scales or emission radii within the same jet system. The long, smooth nature of many precursors aligns physically with emission from cocoon shock breakout occurring at large radii ($R \sim 10^{11}-10^{12}$ cm), an interpretation reinforced by the observed lack of variability and lag. Conversely, short and hard precursors may result from early-stage, magnetically dominated outflows, further supporting a unified two-stage jet emission process.

In summary, our results suggest that the G_1 and G_2 components may originate from distinct physical regimes, likely involving different radiative efficiencies, emission region scales, or dissipation mechanisms, within the same collapsing-star central engine. The precursors are typically generated at larger radii with minimal spectral evolution, while the main pulses arise from smaller radii with significant spectral evolution. Our study highlights the critical importance of a pulse-wise classification scheme in GRBs, as simple duration-based categorization (T_{90}) can be misleading for multi-episode bursts. We recommend using a combination of duration, hardness, MVT, and spectral lag for each pulse to accurately assess physical origin. Future studies will extend this pulse-level analysis to other complex temporal structures, such as short GRBs with extended emission, and incorporate E_p measurements and broader-band spectral fits (e.g., from Fermi/GBM or HXMT) will allow a more subtle test of energy correlations.

An important question beyond the scope of this work is whether the observed differences between precursor and main burst continue evolving in later emission

episodes, such as the second main burst (Component IIb) or extended emission (Component III). Addressing this question requires separate sample selection, as many precursor GRBs lack clear later components. We plan to investigate the temporal evolution of emission properties across multiple episodes systematically in forthcoming papers in this series, examining whether precursors represent a unique initial phase or one end of a continuum that evolves throughout the GRB event. Finally, a few additional comments are worth mentioning regarding the physical interpretation and methodological limitations inherent in separating the precursor (G_1) and main burst (G_2) phases. First, the long minimum variability timescale (Δt_{\min}) and near-zero spectral lag ($\tau \sim 0$) observed for the precursor component are highly consistent with the jet shock breakout model. In this scenario, the precursor signal arises as the relativistic jet punches through the stellar envelope, resulting in quasi-thermal emission from large radii ($R \sim 10^{11}$ – 10^{12} cm). Alternatively, the observed dichotomy could stem from a two-stage jet launching scenario, where a magnetically dominated outflow, emitting a hard, lag-free precursor via magnetic reconnection, precedes a baryonic jet that generates the internal shocks responsible for the main, lag-bearing emission (Zhang et al. 2018). Such a transition would naturally account for the distinct temporal and spectral lag properties observed. Second, we must acknowledge that a portion of the observed MVT difference is attributable to signal-to-noise ratio (SNR) selection effects. Our paired within-burst analysis reveals a strong anti-correlation between $\Delta \log_{10}$ MVT and $\Delta \log_{10} F_p$ ($\beta \simeq -1.07$, $R^2 \simeq 0.75$), implying that the lower flux and poorer SNR of precursors naturally inflate their measurable MVT. However, the existence of a robust subset of events featuring intrinsically bright and short-timescale precursors confirms that the observed MVT separation is not purely an artifact of measurement sensitivity. Third, the relative energetics further support the precursor’s peripheral role: pulses carry only a small fraction of the total prompt fluence, and no distinct afterglow component is observed exclusively in association with the precursor. This is consistent with a relatively low-energy, possibly radiation-dominated outflow that fails to drive a strong external shock. By con-

trast, the main emission accounts for the bulk of the energy release and drives the standard long GRB afterglow. Finally, we caution that our physical radius estimates rely on an assumed, common bulk Lorentz factor Γ , and since $R \propto \Gamma^2$, the absolute values are sensitive to this choice. Moreover, the statistical distinction in spectral lag is only moderate ($p=0.075$) given the current sample size, necessitating future confirmation from a larger set of events. A major limitation is the reliance on the *Swift*/BAT band for spectral analysis. Joint *Swift*+*Fermi* observations covering a broader energy range will be crucial to accurately constrain the spectral peak energy (E_p) and Γ for each phase.

ACKNOWLEDGMENTS

We thank Wang Xiao, Cui Zhi-Li, Xiao Cheng-Long, and Li Wen for carefully verifying the sample data in this study. We also thank Bing Zhang for many useful discussions. LL is supported by the Natural Science Foundation of China (grant No. 11874033), the KC Wong Magna Foundation at Ningbo University, and made use of the High Energy Astrophysics Science Archive Research Center (HEASARC) Online Service at the NASA/Goddard Space Flight Center (GSFC). YFH is supported by the National Natural Science Foundation of China (Grant No. 12233002), by the National Key R&D Program of China (2021YFA0718500). YFH also acknowledges the support from the Xinjiang Tianchi Program. The computations were supported by the high performance computing center at Ningbo University.

Facilities: *Swift*

Software: 3ML (Vianello et al. 2015), `matplotlib` (Hunter 2007), `NumPy` (Harris et al. 2020; van der Walt et al. 2011), `SciPy` (Virtanen et al. 2020), `lmfit` (Newville et al. 2016), `astropy` (Astropy Collaboration et al. 2013), `pandas` (Reback et al. 2022), `emcee` (Foreman-Mackey et al. 2013), `seaborn` (Waskom et al. 2017)

REFERENCES

Ahumada, T., Singer, L. P., Anand, S., et al. 2021, *Nature Astronomy*, 5, 917, doi: [10.1038/s41550-021-01428-7](https://doi.org/10.1038/s41550-021-01428-7)

Amati, L. 2006, *MNRAS*, 372, 233, doi: [10.1111/j.1365-2966.2006.10840.x](https://doi.org/10.1111/j.1365-2966.2006.10840.x)

Amati, L., Frontera, F., Tavani, M., et al. 2002, *A&A*, 390, 81, doi: [10.1051/0004-6361:20020722](https://doi.org/10.1051/0004-6361:20020722)

Astropy Collaboration, Robitaille, T. P., Tollerud, E. J., et al. 2013, *A&A*, 558, A33, doi: [10.1051/0004-6361/201322068](https://doi.org/10.1051/0004-6361/201322068)

Band, D. L. 1997, *ApJ*, 486, 928, doi: [10.1086/304566](https://doi.org/10.1086/304566)

Berger, E. 2014, *ARA&A*, 52, 43, doi: [10.1146/annurev-astro-081913-035926](https://doi.org/10.1146/annurev-astro-081913-035926)

Bernardini, M. G., Ghirlanda, G., Campana, S., et al. 2015, *MNRAS*, 446, 1129, doi: [10.1093/mnras/stu2153](https://doi.org/10.1093/mnras/stu2153)

Bromberg, O., Nakar, E., Piran, T., & Sari, R. 2013, *ApJ*, 764, 179, doi: [10.1088/0004-637X/764/2/179](https://doi.org/10.1088/0004-637X/764/2/179)

Burton, D., Ghirlanda, G., Ghisellini, G., et al. 2008, *ApJL*, 685, L19, doi: [10.1086/592350](https://doi.org/10.1086/592350)

Cheng, L. X., Ma, Y. Q., Cheng, K. S., Lu, T., & Zhou, Y. Y. 1995, *A&A*, 300, 746

Coppin, P., de Vries, K. D., & van Eijndhoven, N. 2020, *PhRvD*, 102, 103014, doi: [10.1103/PhysRevD.102.103014](https://doi.org/10.1103/PhysRevD.102.103014)

Dainotti, M. G., & Amati, L. 2018, *PASP*, 130, 051001, doi: [10.1088/1538-3873/aaa8d7](https://doi.org/10.1088/1538-3873/aaa8d7)

Dezalay, J. P., Barat, C., Talon, R., et al. 1992, in American Institute of Physics Conference Series, Vol. 265, American Institute of Physics Conference Series, ed. W. S. Paciesas & G. J. Fishman, 304

Dezalay, J. P., Barat, C., Talon, R., et al. 1995, *Ap&SS*, 231, 115, doi: [10.1007/BF00658598](https://doi.org/10.1007/BF00658598)

Evans, P. A., Beardmore, A. P., Page, K. L., et al. 2007, *A&A*, 469, 379, doi: [10.1051/0004-6361:20077530](https://doi.org/10.1051/0004-6361:20077530)

—. 2009, *MNRAS*, 397, 1177, doi: [10.1111/j.1365-2966.2009.14913.x](https://doi.org/10.1111/j.1365-2966.2009.14913.x)

Foreman-Mackey, D., Hogg, D. W., Lang, D., & Goodman, J. 2013, *PASP*, 125, 306, doi: [10.1086/670067](https://doi.org/10.1086/670067)

Fynbo, J. P. U., Watson, D., Thöne, C. C., et al. 2006, *Nature*, 444, 1047, doi: [10.1038/nature05375](https://doi.org/10.1038/nature05375)

Gal-Yam, A., Fox, D. B., Price, P. A., et al. 2006, *Nature*, 444, 1053, doi: [10.1038/nature05373](https://doi.org/10.1038/nature05373)

Gehrels, N., Norris, J. P., Barthelmy, S. D., et al. 2006, *Nature*, 444, 1044, doi: [10.1038/nature05376](https://doi.org/10.1038/nature05376)

Goldstein, A., Burgess, J. M., Preece, R. D., et al. 2012, *ApJS*, 199, 19, doi: [10.1088/0067-0049/199/1/19](https://doi.org/10.1088/0067-0049/199/1/19)

Golkhou, V. Z., & Butler, N. R. 2014, *ApJ*, 787, 90, doi: [10.1088/0004-637X/787/1/90](https://doi.org/10.1088/0004-637X/787/1/90)

Golkhou, V. Z., Butler, N. R., & Littlejohns, O. M. 2015, *ApJ*, 811, 93, doi: [10.1088/0004-637X/811/2/93](https://doi.org/10.1088/0004-637X/811/2/93)

Gottlieb, O. 2025, *ApJL*, 992, L3, doi: [10.3847/2041-8213/ae09af](https://doi.org/10.3847/2041-8213/ae09af)

Harris, C. R., Millman, K. J., van der Walt, S. J., et al. 2020, *Nature*, 585, 357, doi: [10.1038/s41586-020-2649-2](https://doi.org/10.1038/s41586-020-2649-2)

Heussaff, V., Atteia, J. L., & Zolnierowski, Y. 2013, *A&A*, 557, A100, doi: [10.1051/0004-6361/201321528](https://doi.org/10.1051/0004-6361/201321528)

Horváth, I., Bagoly, Z., Balázs, L. G., et al. 2010, *ApJ*, 713, 552, doi: [10.1088/0004-637X/713/1/552](https://doi.org/10.1088/0004-637X/713/1/552)

Hu, Y.-D., Liang, E.-W., Xi, S.-Q., et al. 2014, *ApJ*, 789, 145, doi: [10.1088/0004-637X/789/2/145](https://doi.org/10.1088/0004-637X/789/2/145)

Hunter, J. D. 2007, *Computing in Science and Engineering*, 9, 90, doi: [10.1109/MCSE.2007.55](https://doi.org/10.1109/MCSE.2007.55)

Kaneko, Y., Bostancı, Z. F., Göğüş, E., & Lin, L. 2015, *MNRAS*, 452, 824, doi: [10.1093/mnras/stv1286](https://doi.org/10.1093/mnras/stv1286)

Koshut, T. M., Kouveliotou, C., Paciesas, W. S., et al. 1995, *ApJ*, 452, 145, doi: [10.1086/176286](https://doi.org/10.1086/176286)

Kouveliotou, C., Meegan, C. A., Fishman, G. J., et al. 1993, *ApJL*, 413, L101, doi: [10.1086/186969](https://doi.org/10.1086/186969)

Lazzati, D. 2005, *MNRAS*, 357, 722, doi: [10.1111/j.1365-2966.2005.08687.x](https://doi.org/10.1111/j.1365-2966.2005.08687.x)

Li, L. 2019, *ApJS*, 242, 16, doi: [10.3847/1538-4365/ab1b78](https://doi.org/10.3847/1538-4365/ab1b78)

—. 2023, *ApJS*, 266, 31, doi: [10.3847/1538-4365/acc867](https://doi.org/10.3847/1538-4365/acc867)

—. 2025, arXiv e-prints, arXiv:2512.23660, doi: [10.48550/arXiv.2512.23660](https://doi.org/10.48550/arXiv.2512.23660)

Li, L., Ryde, F., Pe'er, A., Yu, H.-F., & Acuner, Z. 2021a, *ApJS*, 254, 35, doi: [10.3847/1538-4365/abee2a](https://doi.org/10.3847/1538-4365/abee2a)

Li, L., & Wang, Y. 2024, *ApJ*, 972, 195, doi: [10.3847/1538-4357/ad2511](https://doi.org/10.3847/1538-4357/ad2511)

Li, L., & Zhang, B. 2021, *ApJS*, 253, 43, doi: [10.3847/1538-4365/abded1](https://doi.org/10.3847/1538-4365/abded1)

Li, L.-X. 2007, *MNRAS*, 380, 621, doi: [10.1111/j.1365-2966.2007.12083.x](https://doi.org/10.1111/j.1365-2966.2007.12083.x)

Li, X. J., Zhang, Z. B., Zhang, X. L., & Zhen, H. Y. 2021b, *ApJS*, 252, 16, doi: [10.3847/1538-4365/ab3fd](https://doi.org/10.3847/1538-4365/ab3fd)

Liang, E., & Zhang, B. 2005, *ApJ*, 633, 611, doi: [10.1086/491594](https://doi.org/10.1086/491594)

Liang, E.-W., Yi, S.-X., Zhang, J., et al. 2010, *ApJ*, 725, 2209, doi: [10.1088/0004-637X/725/2/2209](https://doi.org/10.1088/0004-637X/725/2/2209)

Lien, A., Sakamoto, T., Barthelmy, S. D., et al. 2016, *ApJ*, 829, 7, doi: [10.3847/0004-637X/829/1/7](https://doi.org/10.3847/0004-637X/829/1/7)

McBreen, S., Hanlon, L., McGlynn, S., et al. 2006, *A&A*, 455, 433, doi: [10.1051/0004-6361:20065203](https://doi.org/10.1051/0004-6361:20065203)

Nakar, E., & Piran, T. 2002, *MNRAS*, 330, 920, doi: [10.1046/j.1365-8711.2002.05136.x](https://doi.org/10.1046/j.1365-8711.2002.05136.x)

Nakar, E., & Sari, R. 2012, *ApJ*, 747, 88, doi: [10.1088/0004-637X/747/2/88](https://doi.org/10.1088/0004-637X/747/2/88)

Newville, M., Stensitzki, T., Allen, D. B., et al. 2016, *ascl*, ascl

Norris, J. P., & Bonnell, J. T. 2006, *ApJ*, 643, 266, doi: [10.1086/502796](https://doi.org/10.1086/502796)

Norris, J. P., Bonnell, J. T., Kazanas, D., et al. 2005, *ApJ*, 627, 324, doi: [10.1086/430294](https://doi.org/10.1086/430294)

Norris, J. P., Marani, G. F., & Bonnell, J. T. 2000, *ApJ*, 534, 248, doi: [10.1086/308725](https://doi.org/10.1086/308725)

Pe'er, A., Ryde, F., Wijers, R. A. M. J., Mészáros, P., & Rees, M. J. 2007, *ApJL*, 664, L1, doi: [10.1086/520534](https://doi.org/10.1086/520534)

Planck Collaboration, Aghanim, N., Akrami, Y., et al. 2018, arXiv e-prints, arXiv:1807.06209, <https://arxiv.org/abs/1807.06209>

Qin, Y., Liang, E.-W., Liang, Y.-F., et al. 2013, *ApJ*, 763, 15, doi: [10.1088/0004-637X/763/1/15](https://doi.org/10.1088/0004-637X/763/1/15)

Rastinejad, J. C., Gompertz, B. P., Levan, A. J., et al. 2022, *Nature*, 612, 223, doi: [10.1038/s41586-022-05390-w](https://doi.org/10.1038/s41586-022-05390-w)

Reback, J., jbrockmendel, McKinney, W., et al. 2022, *pandas-dev/pandas*: Pandas 1.4.2, v1.4.2, Zenodo, Zenodo, doi: [10.5281/zenodo.3509134](https://doi.org/10.5281/zenodo.3509134)

Sakamoto, T., Barthelmy, S. D., Baumgartner, W. H., et al. 2011, *ApJS*, 195, 2, doi: [10.1088/0067-0049/195/1/2](https://doi.org/10.1088/0067-0049/195/1/2)

Troja, E., Fryer, C. L., O'Connor, B., et al. 2022, *Nature*, 612, 228, doi: [10.1038/s41586-022-05327-3](https://doi.org/10.1038/s41586-022-05327-3)

Ukwatta, T. N., Stamatikos, M., Dhuga, K. S., et al. 2010, *ApJ*, 711, 1073, doi: [10.1088/0004-637X/711/2/1073](https://doi.org/10.1088/0004-637X/711/2/1073)

van der Walt, S., Colbert, S. C., & Varoquaux, G. 2011, *Computing in Science and Engineering*, 13, 22, doi: [10.1109/MCSE.2011.37](https://doi.org/10.1109/MCSE.2011.37)

Vianello, G., Lauer, R. J., Younk, P., et al. 2015, arXiv e-prints, arXiv:1507.08343, doi: [10.48550/arXiv.1507.08343](https://doi.org/10.48550/arXiv.1507.08343)

Virtanen, P., Gommers, R., Oliphant, T. E., et al. 2020, *Nature Methods*, 17, 261, doi: [10.1038/s41592-019-0686-2](https://doi.org/10.1038/s41592-019-0686-2)

Wang, X.-Y., & Mészáros, P. 2007, *ApJ*, 670, 1247, doi: [10.1086/522820](https://doi.org/10.1086/522820)

Waskom, M., Botvinnik, O., O'Kane, D., et al. 2017, *Mwaskom/Seaborn*: V0.8.1 (September 2017), v0.8.1, Zenodo, Zenodo, doi: [10.5281/zenodo.883859](https://doi.org/10.5281/zenodo.883859)

Woosley, S. E., & Bloom, J. S. 2006, *ARA&A*, 44, 507, doi: [10.1146/annurev.astro.43.072103.150558](https://doi.org/10.1146/annurev.astro.43.072103.150558)

Xu, M., & Huang, Y. F. 2012, *A&A*, 538, A134, doi: [10.1051/0004-6361/201117754](https://doi.org/10.1051/0004-6361/201117754)

Yang, J., Ai, S., Zhang, B.-B., et al. 2022, *Nature*, 612, 232, doi: [10.1038/s41586-022-05403-8](https://doi.org/10.1038/s41586-022-05403-8)

Yi, T., Liang, E., Qin, Y., & Lu, R. 2006, *MNRAS*, 367, 1751, doi: [10.1111/j.1365-2966.2006.10083.x](https://doi.org/10.1111/j.1365-2966.2006.10083.x)

Yonetoku, D., Murakami, T., Nakamura, T., et al. 2004, *ApJ*, 609, 935, doi: [10.1086/421285](https://doi.org/10.1086/421285)

Yonetoku, D., Murakami, T., Tsutsui, R., et al. 2010, *PASJ*, 62, 1495, doi: [10.1093/pasj/62.6.1495](https://doi.org/10.1093/pasj/62.6.1495)

Zhang, B. 2011, *Comptes Rendus Physique*, 12, 206, doi: [10.1016/j.crhy.2011.03.004](https://doi.org/10.1016/j.crhy.2011.03.004)

Zhang, B., Zhang, B.-B., Virgili, F. J., et al. 2009, *ApJ*, 703, 1696, doi: [10.1088/0004-637X/703/2/1696](https://doi.org/10.1088/0004-637X/703/2/1696)

Zhang, B.-B., Zhang, B., Castro-Tirado, A. J., et al. 2018, *Nature Astronomy*, 2, 69, doi: [10.1038/s41550-017-0309-8](https://doi.org/10.1038/s41550-017-0309-8)

Zhang, B. B., Liu, Z. K., Peng, Z. K., et al. 2021, *Nature Astronomy*, 5, 911, doi: [10.1038/s41550-021-01395-z](https://doi.org/10.1038/s41550-021-01395-z)

Zhang, F.-W., Shao, L., Yan, J.-Z., & Wei, D.-M. 2012, *ApJ*, 750, 88, doi: [10.1088/0004-637X/750/2/88](https://doi.org/10.1088/0004-637X/750/2/88)

Zou, Y.-C., & Piran, T. 2010, *MNRAS*, 402, 1854, doi: [10.1111/j.1365-2966.2009.15863.x](https://doi.org/10.1111/j.1365-2966.2009.15863.x)

Table 1. Temporal properties of the precursor (G_1) and main emission (G_2) sub-bursts in our GRB sample. Each entry lists the time bin resolution used, the start and end times ($t_1 \sim t_2$), total pulse width, T_{90} duration with asymmetric errors, pulse peak time (t_p), and peak count rate (F_p) with 1σ uncertainties. These values form the basis for the duration and gap analyses presented in Section 3.1.

GRB	Sub-burst	Time bin (ms)	$t_1 \sim t_2$ (s)	T_{pulse} (s)	t_p (s)	F_p	Classified as (PE or ME)
050820A	G_1	256	$-3.35 \sim 22.50$	25.86	0.49	0.16 ± 0.02	PE
	G_2	256	$223.72 \sim 241.13$	17.41	229.61	0.38 ± 0.04	ME
060923A	G_1	1024	$-43.22 \sim -29.91$	13.31	-39.13	0.07 ± 0.02	PE
	G_2	1024	$-6.36 \sim 16.17$	22.53	-0.22	0.14 ± 0.02	ME
061007	G_1	256	$-3.78 \sim 14.90$	18.69	0.31	0.83 ± 0.07	PE
	G_2	256	$20.02 \sim 69.94$	49.92	45.88	2.12 ± 0.05	ME
061121	G_1	256	$-2.28 \sim 10.01$	12.29	2.84	0.25 ± 0.02	PE
	G_2	256	$51.99 \sim 102.68$	50.69	74.78	3.15 ± 0.05	ME
061121	G_1	256	$-2.28 \sim 10.01$	12.29	2.84	0.25 ± 0.02	PE
	G_2	256	$51.99 \sim 102.68$	50.69	74.78	3.15 ± 0.05	ME
061202	G_1	1024	$-2.76 \sim 11.58$	14.34	1.34	0.04 ± 0.01	PE
	G_2	1024	$66.87 \sim 121.14$	54.27	75.06	0.33 ± 0.01	ME
061222A	G_1	256	$23.92 \sim 30.58$	6.66	25.71	0.35 ± 0.03	PE
	G_2	256	$53.36 \sim 100.46$	47.10	88.43	1.35 ± 0.04	ME
070306	G_1	1024	$-8.56 \sim 25.23$	33.79	10.9	0.11 ± 0.02	PE
	G_2	1024	$78.48 \sim 157.33$	78.85	97.94	0.44 ± 0.01	ME
070521	G_1	256	$-6.36 \sim 5.93$	12.29	0.30	0.31 ± 0.03	PE
	G_2	256	$8.23 \sim 45.35$	37.12	31.02	1.10 ± 0.04	ME
071010B	G_1	1024	$-37.54 \sim -6.82$	30.72	-24.23	0.06 ± 0.01	PE
	G_2	256	$-2.98 \sim 20.31$	23.30	2.14	0.89 ± 0.03	ME
080928	G_1	1024	$-5.53 \sim 3.69$	9.22	-4.5	0.04 ± 0.01	PE
	G_2	1024	$195.18 \sim 257.64$	62.46	202.34	0.21 ± 0.01	ME
090618	G_1	256	$-7.63 \sim 41.78$	49.41	9.52	0.79 ± 0.04	PE
	G_2	256	$42.03 \sim 159.79$	117.76	65.84	4.65 ± 0.07	ME
091208B	G_1	256	$-0.72 \sim 4.40$	5.12	0.30	0.59 ± 0.09	PE
	G_2	256	$5.17 \sim 13.36$	8.19	8.24	2.16 ± 0.14	ME
121128A	G_1	256	$-1.57 \sim 3.04$	4.61	0.22	0.11 ± 0.03	PE
	G_2	256	$9.18 \sim 41.70$	32.51	21.73	1.80 ± 0.05	ME
140206A	G_1	256	$-1.44 \sim 24.93$	26.37	6.24	1.42 ± 0.04	PE
	G_2	256	$50.02 \sim 90.72$	40.70	61.02	3.44 ± 0.06	ME

Table 1. — continued

GRB	Sub-burst	Time bin (ms)	$t_1 \sim t_2$ (s)	T_{pulse} (s)	t_{p} (s)	F_{p}	Classified as (PE or ME)
140512A	G_1	256	$-16.50 \sim 10.13$	26.62	1.68	0.52 ± 0.05	PE
	G_2	256	$91.02 \sim 166.29$	75.26	122.51	0.97 ± 0.04	ME
140629A	G_1	1024	$-9.13 \sim 9.30$	18.43	0.09	0.19 ± 0.02	PE
	G_2	1024	$10.33 \sim 30.81$	20.48	12.38	0.51 ± 0.03	ME
150323A	G_1	1024	$-5.53 \sim 24.17$	29.7	2.66	0.12 ± 0.02	PE
	G_2	256	$121.45 \sim 155.75$	34.3	131.94	0.58 ± 0.03	ME
160131A	G_1	256	$-2.18 \sim 7.81$	9.98	5.50	0.16 ± 0.03	PE
	G_2	256	$8.06 \sim 114.05$	105.98	16.77	0.88 ± 0.05	ME
160703A	G_1	256	$-26.98 \sim -18.53$	8.45	-25.18	0.12 ± 0.02	PE
	G_2	256	$-14.43 \sim 45.22$	59.65	27.30	0.77 ± 0.03	ME
180325A	G_1	256	$-0.93 \sim 8.29$	9.22	1.12	0.31 ± 0.03	PE
	G_2	256	$72.29 \sim 103.01$	30.72	80.74	1.45 ± 0.05	ME
180728A	G_1	256	$-1.74 \sim 6.97$	8.7	0.82	0.49 ± 0.04	PE
	G_2	16	$11.10 \sim 23.43$	12.34	12.87	17.46 ± 0.71	ME
190324A	G_1	256	$-0.66 \sim 5.22$	5.89	0.62	0.17 ± 0.04	PE
	G_2	256	$16.49 \sim 43.62$	27.14	24.17	1.65 ± 0.07	ME

Table 2. Comparative analysis of precursor and main emission properties for each GRB in the sample.

GRB	z	t_{gap} (s)	$t_{\text{gap}}/(1+z)$ (s)	$R_{t_{90}}$	R_{F_p}	R_{HR}	R_{MVT}	R_{τ}
(1)	(2)	(3)	(4)	(5)	(6)	(7)	(8)	(9)
050820A	2.612	201.2 ± 3.4	55.7 ± 1.0	1.54 ± 0.26	0.42 ± 0.07	0.65 ± 0.12	1.19 ± 0.75	0.75 ± 0.08
060923A	2.800	23.6 ± 3.7	6.2 ± 1.0	0.63 ± 0.15	0.50 ± 0.16	0.64 ± 0.31	2.01 ± 1.77	0.67 ± 0.03
061007	1.260	~ 5.1	2.3 ± 3.8	0.40 ± 0.13	0.39 ± 0.03	0.98 ± 0.04	1.96 ± 4.28	4.00 ± 0.80
061121	1.314	42.0 ± 10.3	18.1 ± 4.4	0.36 ± 0.23	0.08 ± 0.01	0.87 ± 0.11	8.15 ± 2.88	-2.69 ± 1.02
061202	2.253	55.3 ± 6.0	17.0 ± 1.8	0.29 ± 0.09	0.12 ± 0.03	0.28 ± 0.49	6.46 ± 5.35	-1.75 ± 0.15
061222A	2.088	22.8 ± 5.9	7.4 ± 1.9	0.14 ± 0.04	0.26 ± 0.02	0.79 ± 0.07	1.03 ± 1.92	-1.64 ± 0.30
070306	1.496	53.2 ± 8.8	21.3 ± 3.5	0.44 ± 0.13	0.25 ± 0.05	1.35 ± 0.45	18.05 ± 8.77	-1.30 ± 0.51
070521	2.087	~ 2.3	0.7 ± 2.0	0.40 ± 0.15	0.28 ± 0.03	0.85 ± 0.07	1.96 ± 2.46	3.15 ± 0.43
071010B	0.947	~ 3.8	2.0 ± 2.1	1.71 ± 0.58	0.07 ± 0.01	1.06 ± 0.17	3.61 ± 1.15	-3.14 ± 2.39
080928	1.690	191.5 ± 7.4	71.2 ± 2.7	0.16 ± 0.03	0.19 ± 0.05	0.91 ± 1.40	4.30 ± 1.31	-11.92 ± 1.21
090618	0.540	~ 0.2	0.2 ± 9.6	0.51 ± 0.20	0.17 ± 0.01	1.21 ± 0.03	2.33 ± 4.19	8.22 ± 2.65
091208B	1.063	~ 0.8	0.4 ± 1.1	0.83 ± 0.35	0.27 ± 0.05	0.85 ± 0.32	1.66 ± 3.53	0.55 ± 0.38
121128A	2.200	~ 6.1	1.9 ± 1.4	0.13 ± 0.05	0.06 ± 0.02	0.28 ± 0.59	13.34 ± 3.45	27.75 ± 14.94
140206A	2.730	25.1 ± 8.4	6.7 ± 2.2	0.88 ± 0.52	0.41 ± 0.01	0.99 ± 0.05	0.37 ± 0.15	0.44 ± 0.29
140512A	0.725	80.9 ± 8.9	46.9 ± 5.2	0.39 ± 0.12	0.54 ± 0.06	1.36 ± 0.19	12.16 ± 8.07	-11.79 ± 1.92
140629A	2.275	~ 1.0	0.3 ± 1.0	1.00 ± 0.42	0.37 ± 0.04	0.94 ± 0.35	1.29 ± 0.51	1.46 ± 0.23
150323A	0.593	97.3 ± 5.8	61.1 ± 3.7	0.85 ± 0.26	0.21 ± 0.04	1.36 ± 0.38	23.37 ± 15.30	2.80 ± 1.26
160131A	0.972	~ 0.3	0.1 ± 2.8	0.10 ± 0.02	0.18 ± 0.04	0.85 ± 0.24	0.87 ± 1.59	\dots
160703A	1.500	~ 4.1	1.6 ± 4.5	0.17 ± 0.05	0.16 ± 0.03	0.93 ± 0.34	4.11 ± 8.24	12.25 ± 4.20
180325A	2.248	64.0 ± 3.6	19.7 ± 1.1	0.32 ± 0.11	0.21 ± 0.02	0.57 ± 0.10	6.57 ± 1.72	1.75 ± 1.64
180728A	0.117	3.3 ± 2.2	3.0 ± 2.0	0.64 ± 0.47	0.03 ± 0.00	0.62 ± 0.18	21.21 ± 3.17	3.18 ± 0.66
190324A	1.171	11.3 ± 2.4	5.2 ± 1.1	0.29 ± 0.11	0.10 ± 0.02	0.77 ± 0.46	22.16 ± 16.27	-5.44 ± 0.53

NOTE—Listed quantities include the redshift, observed-frame quiescent gap duration and its rest-frame corrected value, and the ratios of precursor to main emission in terms of T_{90} , F_p , HR, MVT, and spectral lag. These values support the classification and consistency testing discussed in Sections 3.1–3.4.

Table 3. Individual T_{90} durations (15–150 keV) of precursor and main emission sub-bursts for each GRB. All components in the sample satisfy the long-burst ($T_{90} > 2$ s) classification. This supports the conclusion that both precursor and main emission episodes generally belong to the Type II GRB population based on duration alone.

GRB	Precursor (G_1)		Main emission (G_2)	
	Value	Classification	Value	Classification
050820A	$21.2^{+2.6}_{-2.0}$ [s]	Long	$13.8^{+1.3}_{-2.3}$ [s]	Long
060923A	$10.2^{+2.0}_{-1.0}$ [s]	Long	$16.4^{+3.1}_{-3.1}$ [s]	Long
061007	$13.3^{+2.8}_{-2.6}$ [s]	Long	$33.3^{+8.4}_{-8.2}$ [s]	Long
061121	$8.2^{+2.3}_{-1.8}$ [s]	Long	$23.0^{+17.7}_{-10.0}$ [s]	Long
061202	$10.2^{+3.1}_{-1.0}$ [s]	Long	$35.8^{+13.3}_{-5.1}$ [s]	Long
061222A	$4.9^{+0.8}_{-1.0}$ [s]	Long	$34.6^{+6.7}_{-5.9}$ [s]	Long
070306	$24.6^{+5.1}_{-4.1}$ [s]	Long	$55.3^{+16.4}_{-7.2}$ [s]	Long
070521	$9.0^{+1.3}_{-2.0}$ [s]	Long	$22.5^{+8.7}_{-5.9}$ [s]	Long
071010B	$24.6^{+3.1}_{-3.1}$ [s]	Long	$14.3^{+6.1}_{-2.8}$ [s]	Long
080928	$7.7^{+0.5}_{-1.0}$ [s]	Long	$48.1^{+10.2}_{-4.1}$ [s]	Long
090618	$35.1^{+8.2}_{-6.1}$ [s]	Long	$69.4^{+36.1}_{-12.3}$ [s]	Long
091208B	$3.8^{+0.8}_{-0.5}$ [s]	Long	$4.6^{+1.5}_{-2.0}$ [s]	Long
121128A	$2.8^{+1.0}_{-0.8}$ [s]	Long	$22.5^{+5.6}_{-4.3}$ [s]	Long
140206A	$17.4^{+7.2}_{-1.8}$ [s]	Long	$19.7^{+16.6}_{-4.3}$ [s]	Long
140512A	$19.7^{+2.8}_{-4.1}$ [s]	Long	$50.7^{+16.1}_{-8.4}$ [s]	Long
140629A	$12.3^{+3.1}_{-3.1}$ [s]	Long	$12.3^{+7.2}_{-1.0}$ [s]	Long
150323A	$20.5^{+5.1}_{-4.1}$ [s]	Long	$24.1^{+7.4}_{-2.8}$ [s]	Long
160131A	$8.2^{+1.0}_{-0.8}$ [s]	Long	$81.4^{+19.2}_{-5.4}$ [s]	Long
160703A	$6.7^{+1.0}_{-0.8}$ [s]	Long	$39.2^{+9.2}_{-11.3}$ [s]	Long
180325A	$6.4^{+1.8}_{-1.0}$ [s]	Long	$20.0^{+7.7}_{-3.1}$ [s]	Long
180728A	$5.4^{+1.8}_{-1.5}$ [s]	Long	$8.4^{+10.0}_{-1.3}$ [s]	Long
190324A	$4.6^{+0.5}_{-0.8}$ [s]	Long	$16.1^{+8.7}_{-2.3}$ [s]	Long

Table 4. Hardness ratios [HR = $\frac{S_{50-100 \text{ keV}}}{S_{25-50 \text{ keV}}}$] for each precursor (G_1) and main emission (G_2) pulse in the sample, computed from background-subtracted fluences in the specified BAT bands. Classification is based on the T_{90} –HR location in the duration–hardness diagram. All episodes are consistent with Type II (long) GRBs in both duration and spectral hardness.

GRB	Precursor (G_1)		Main emission (G_2)	
	Value	Classification	Value	Classification
050820A	0.66±0.10	Long	1.01±0.10	Long
060923A	0.70±0.30	Long	1.09±0.25	Long
061007	1.06±0.04	Long	1.08±0.01	Long
061121	0.72±0.09	Long	0.83±0.01	Long
061202	0.21±0.37	Long	0.76±0.05	Long
061222A	0.70±0.06	Long	0.89±0.01	Long
070306	0.92±0.30	Long	0.68±0.05	Long
070521	0.76±0.06	Long	0.89±0.02	Long
071010B	0.55±0.09	Long	0.52±0.01	Long
080928	0.53±0.81	Long	0.58±0.09	Long
090618	0.85±0.02	Long	0.70±0.00	Long
091208B	0.58±0.19	Long	0.68±0.12	Long
121128A	0.16±0.34	Long	0.58±0.02	Long
140206A	0.81±0.04	Long	0.82±0.02	Long
140512A	1.16±0.16	Long	0.85±0.03	Long
140629A	0.62±0.21	Long	0.66±0.11	Long
150323A	0.83±0.23	Long	0.61±0.03	Long
160131A	0.82±0.23	Long	0.96±0.03	Long
160703A	0.77±0.28	Long	0.83±0.03	Long
180325A	0.59±0.10	Long	1.03±0.05	Long
180728A	0.38±0.11	Long	0.61±0.01	Long
190324A	0.60±0.36	Long	0.78±0.04	Long

Table 5. Minimum variability timescales (Δt_{\min}) of precursors (G_1) and main emissions (G_2) for GRBs in the sample. Values were determined using the Haar wavelet method applied to *Swift*/BAT light curves. All episodes are classified as Type II based on MVT– T_{90} distributions, but precursors tend to exhibit significantly longer MVTs than their corresponding main bursts.

GRB	Precursor (G_1)		Main emission (G_2)	
	Value	Classification	Value	Classification
050820A	(439±214) [ms]	Long	(369±147) [ms]	Long
060923A	(3056±854) [ms]	Long	(1519±1270) [ms]	Long
061007	(700±499) [ms]	Long	(357±135) [ms]	Long
061121	(411±43) [ms]	Long	(50±17) [ms]	Long
061202	(3075±1140) [ms]	Long	(476±353) [ms]	Long
061222A	(409±62) [ms]	Long	(396±134) [ms]	Long
070306	(2802±1288) [ms]	Long	(155±24) [ms]	Long
070521	(1047±97) [ms]	Long	(534±270) [ms]	Long
071010B	(3578±1140) [ms]	Long	(990±20) [ms]	Long
080928	(814±233) [ms]	Long	(189±19) [ms]	Long
090618	(2452±1400) [ms]	Long	(1051±105) [ms]	Long
091208B	(581±209) [ms]	Long	(350±135) [ms]	Long
121128A	(1329±265) [ms]	Long	(100±16) [ms]	Long
140206A	(36±11) [ms]	Long	(96±23) [ms]	Long
140629A	(1074±154) [ms]	Long	(833±305) [ms]	Long
140512A	(480±192) [ms]	Long	(39±21) [ms]	Long
150323A	(4312±1118) [ms]	Long	(185±111) [ms]	Long
160131A	(2161±416) [ms]	Long	(2476±1491) [ms]	Long
160703A	(1942±577) [ms]	Long	(472±209) [ms]	Long
180325A	(775±88) [ms]	Long	(118±28) [ms]	Long
180728A	(692±43) [ms]	Long	(33±4) [ms]	Long
190324A	(1901±294) [ms]	Long	(86±62) [ms]	Long

Table 6. Spectral lags between the 25–50 keV and 15–25 keV bands for individual bursts in the sample. Positive values indicate that the 25–50 keV band peaks earlier than the 15–25 keV band (i.e., high energy leads). Uncertainties are 1σ . Columns list the lag for the main emission (G_1) and the extended emission (G_2), together with the duration-based classification.

GRB	Precursor (G_1)		Main emission (G_2)	
	Value	Classification	Value	Classification
050820A	(480.0 \pm 27.5) [ms]	Long	(640.0 \pm 57.0) [ms]	Long
060923A	(131.2 \pm 3.7) [ms]	Long	(195.2 \pm 5.1) [ms]	Long
061007	(73.6 \pm 12.5) [ms]	Long	(18.4 \pm 1.9) [ms]	Long
061121	(-105.6 \pm 14.7) [ms]	Long	(39.2 \pm 13.8) [ms]	Long
061202	(-480.0 \pm 27.5) [ms]	Long	(273.6 \pm 17.3) [ms]	Long
061222A	(-72.0 \pm 10.7) [ms]	Long	(44.0 \pm 4.6) [ms]	Long
070306	(-364.8 \pm 60.2) [ms]	Long	(281.6 \pm 101.8) [ms]	Long
070521	(131.2 \pm 10.2) [ms]	Long	(41.6 \pm 4.6) [ms]	Long
071010B	(-70.4 \pm 25.6) [ms]	Long	(22.4 \pm 15.0) [ms]	Long
080928	(-1984.0 \pm 32.0) [ms]	Long	(166.4 \pm 16.6) [ms]	Long
090618	(604.8 \pm 12.0) [ms]	Long	(73.6 \pm 23.7) [ms]	Long
091208B	(19.2 \pm 12.8) [ms]	Long	(35.2 \pm 8.0) [ms]	Long
121128A	(710.4 \pm 21.1) [ms]	Long	(25.6 \pm 13.8) [ms]	Long
140206A	(25.6 \pm 15.4) [ms]	Long	(57.6 \pm 16.0) [ms]	Long
140512A	(-716.8 \pm 34.6) [ms]	Long	(60.8 \pm 9.4) [ms]	Long
140629A	(163.2 \pm 7.7) [ms]	Long	(112.0 \pm 16.6) [ms]	Long
150323A	(-358.4 \pm 143.4) [ms]	Long	(-128.0 \pm 26.2) [ms]	Long
160131A	...	Long	(-22.4 \pm 7.0) [ms]	Long
160703A	(470.4 \pm 13.8) [ms]	Long	(38.4 \pm 13.1) [ms]	Long
180325A	(179.2 \pm 94.7) [ms]	Long	(102.4 \pm 79.4) [ms]	Long
180728A	(-198.4 \pm 25.6) [ms]	Long	(-62.4 \pm 10.1) [ms]	Long
190324A	(-156.8 \pm 12.5) [ms]	Long	(28.8 \pm 1.6) [ms]	Long

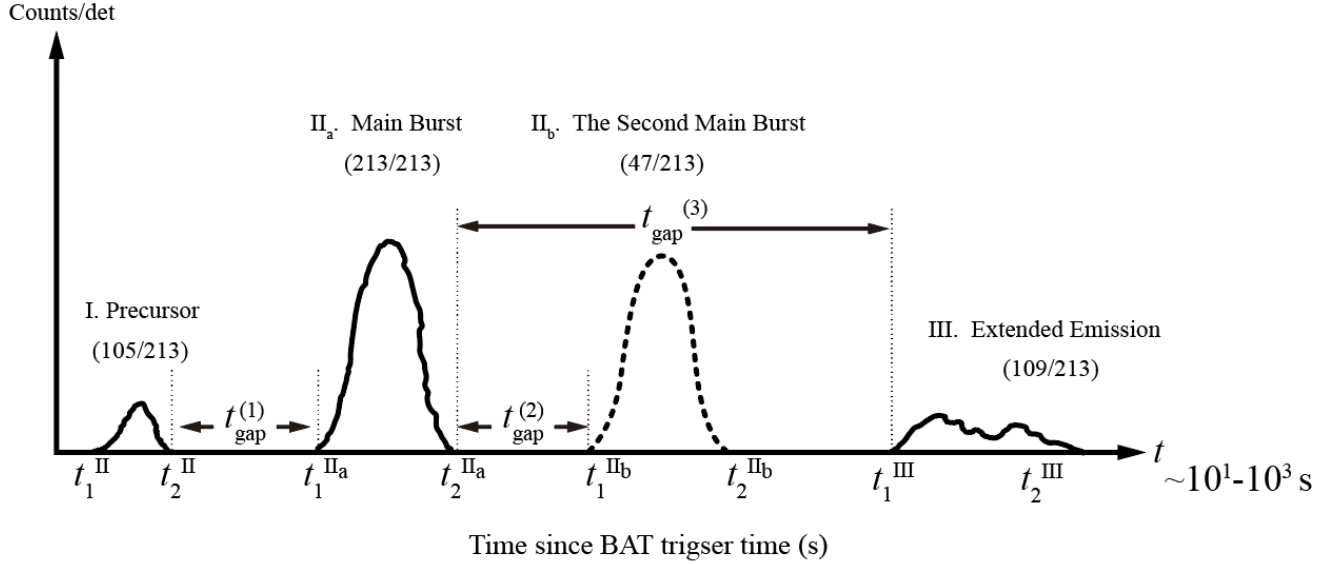


Figure 1. Synthetic schematic light curve illustrating the prompt-emission temporal morphology of *Swift*-BAT GRBs with measured redshift. Four components are identified. I. *Precursor*, a weaker early-time emission episode. IIa. *Main burst*, the first main burst emission episode. IIb. *The second main burst*, a subsequent main burst emission episode with an intensity comparable to IIa, separated from IIa by a clear quiescent gap. III. *Extended emission*, a late and weaker extended emission tail. Quiescent gaps are denoted as $t_{\text{gap}}^{(1)}$ between the precursor and the main burst, $t_{\text{gap}}^{(2)}$ between the first and the second main bursts, and $t_{\text{gap}}^{(3)}$ between the second main burst and the extended emission. The time axis is the observer-frame time in seconds since the BAT trigger.

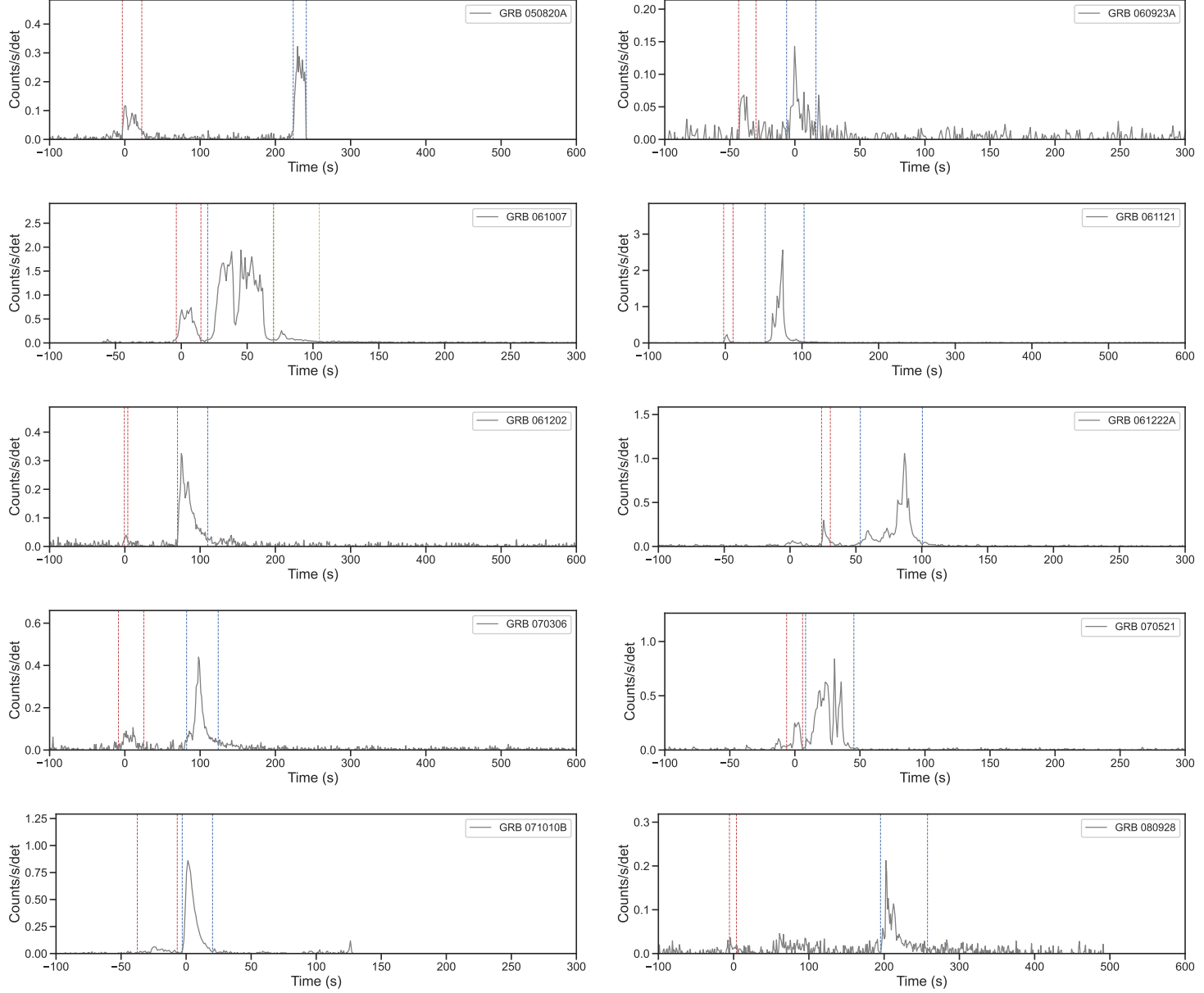
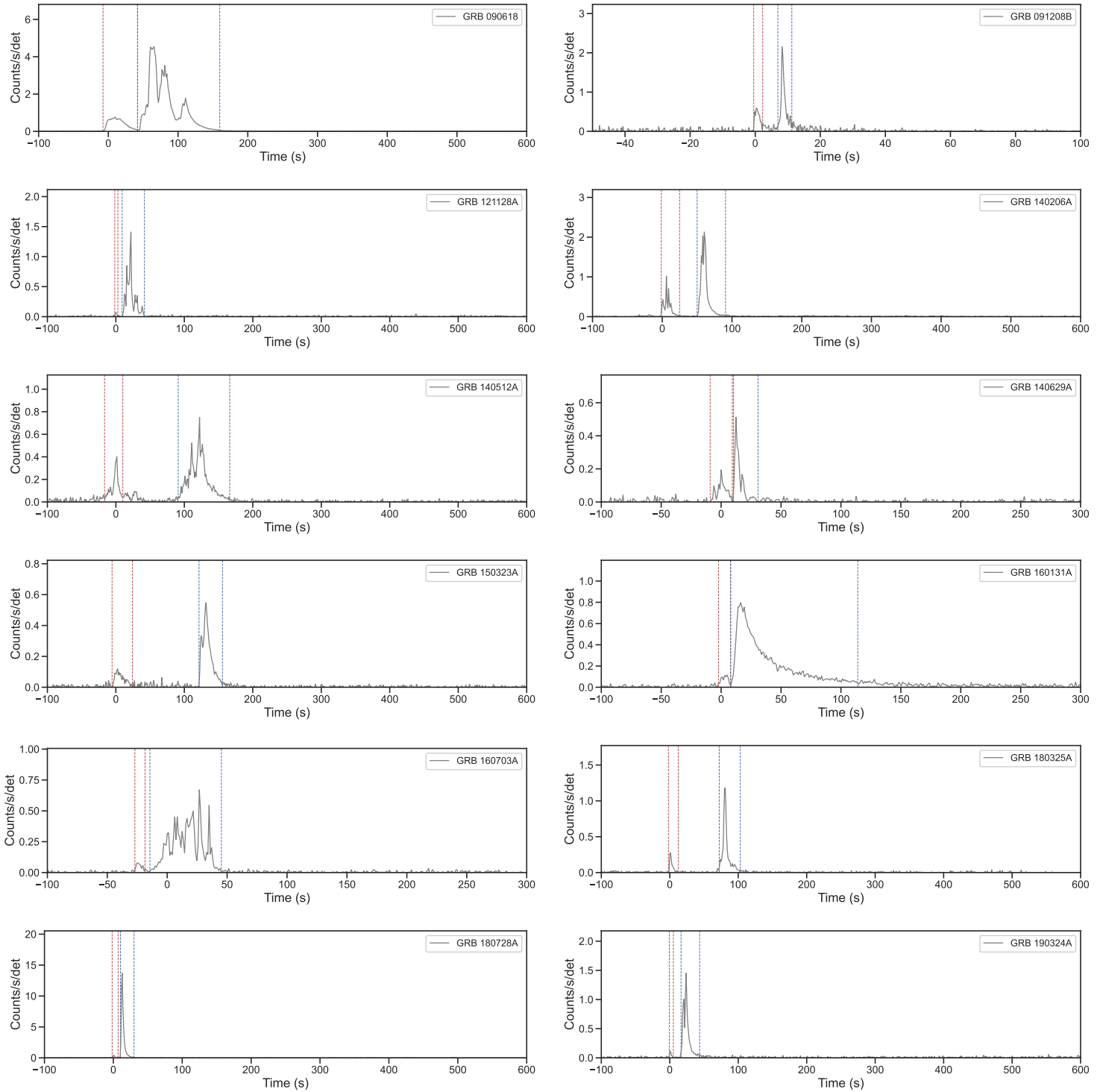


Figure 2. Mask-weighted *Swift*/BAT light curves for the GRBs in our sample. Each panel shows a prompt emission consisting of a precursor (G_1 , indicated by red dashed lines) followed by a main emission (G_2 , blue dashed lines). The quiescent interval between the two components is clearly visible and corresponds to a return to background-level count rates. These double-pulse structures define our Gold sample and motivate the statistical analyses in this work.



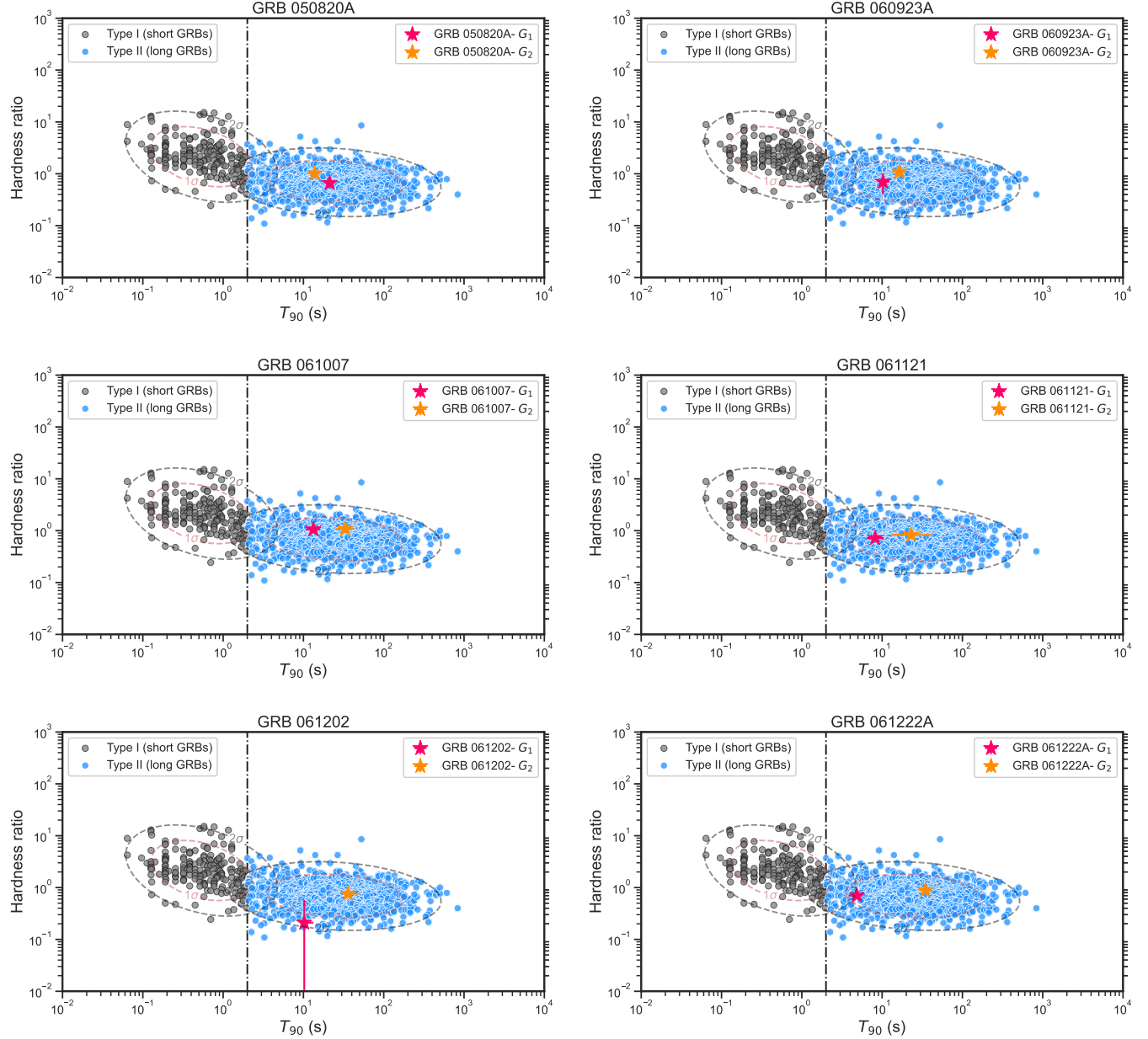
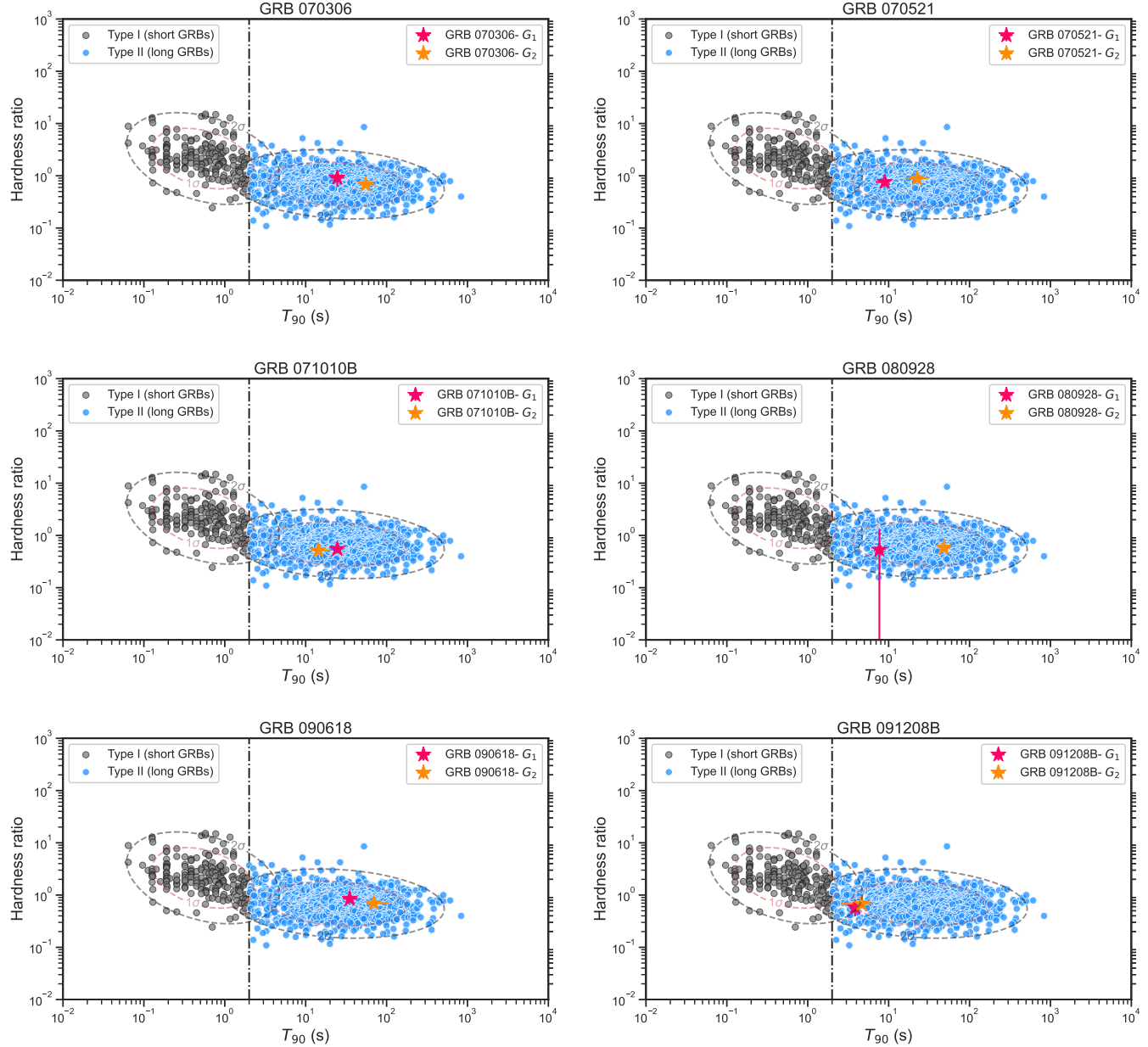
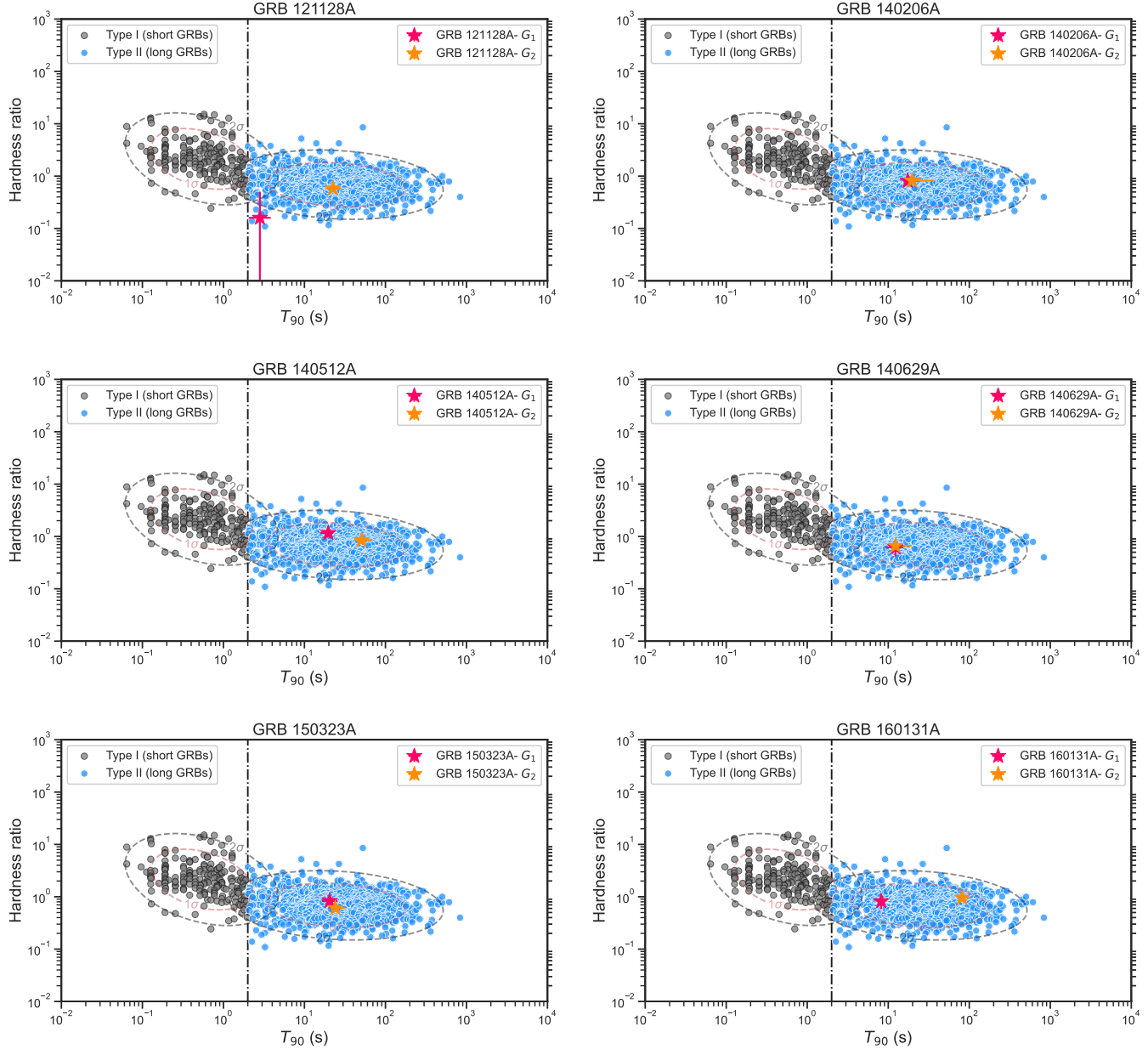
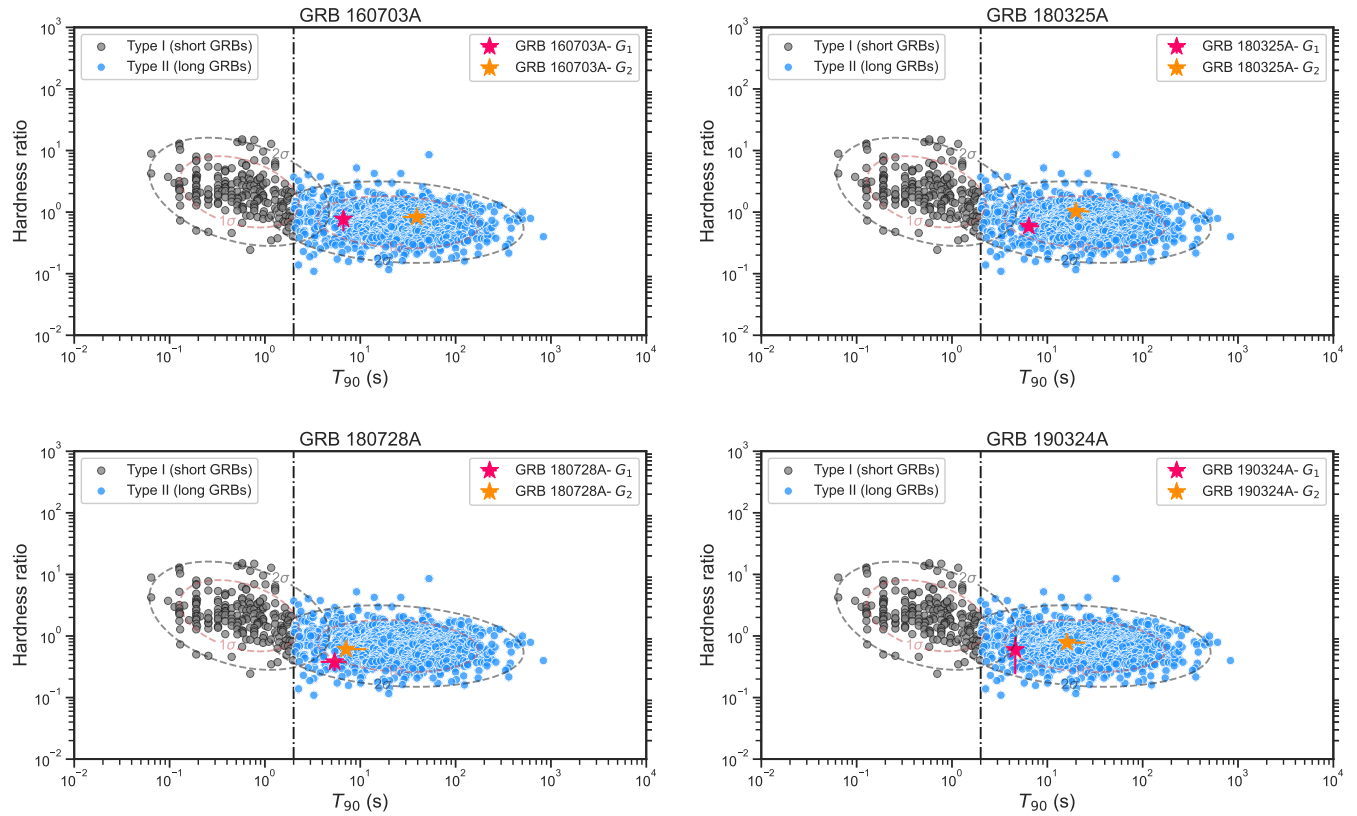


Figure 3. Duration–hardness ratio diagrams for eleven representative GRBs in our sample. Each panel overlays the precursor (G_1 , magenta star) and main emission (G_2 , orange star) atop the broader *Swift* GRB population from Horváth et al. (2010), color-coded by Type I (short; black) and Type II (long; blue). The 1σ ellipses correspond to the bivariate normal fits for each class (see Section 2.2). Both components of each GRB lie within the long GRB region, showing comparable spectral hardness consistent with collapsar-type events.







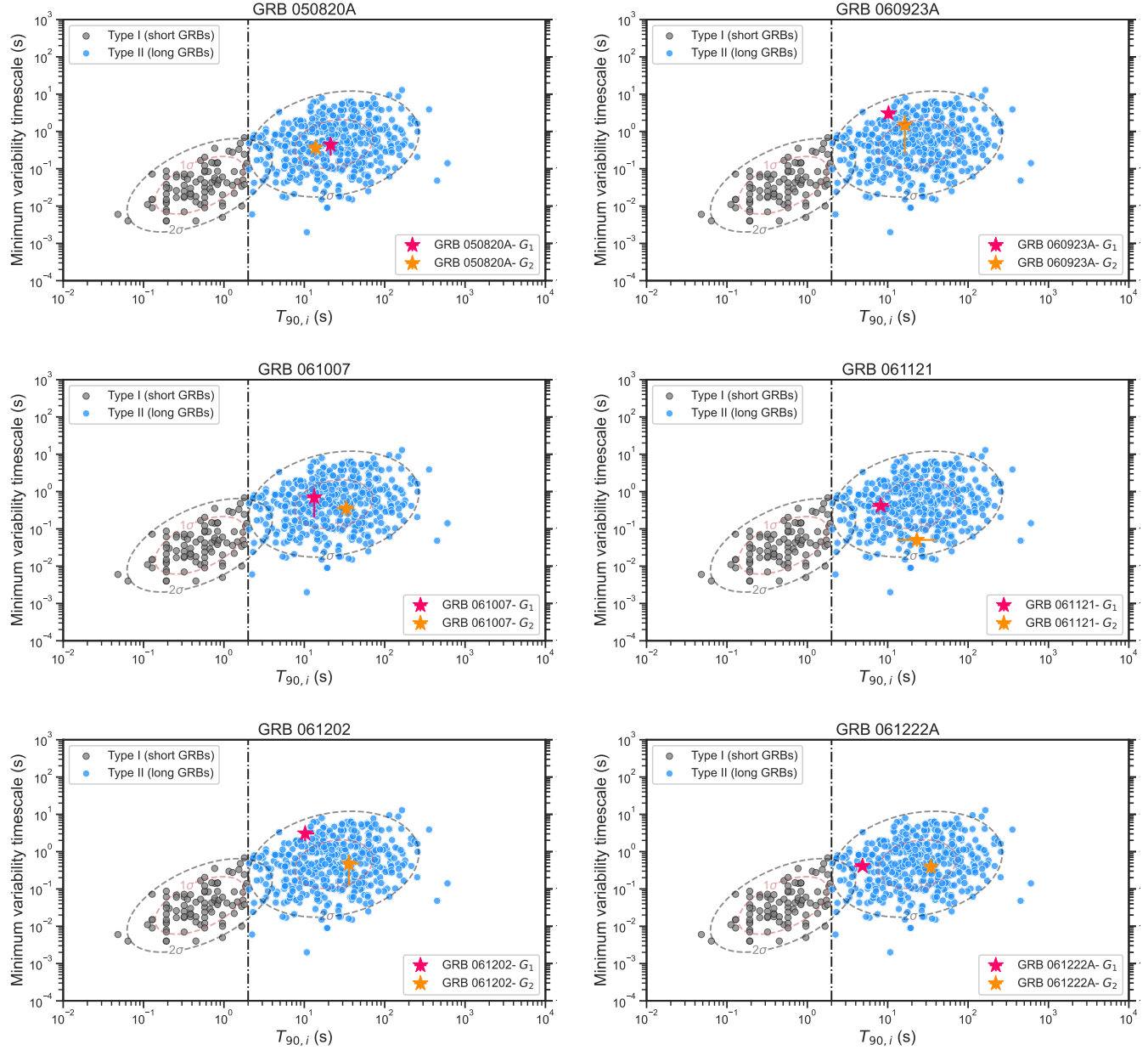
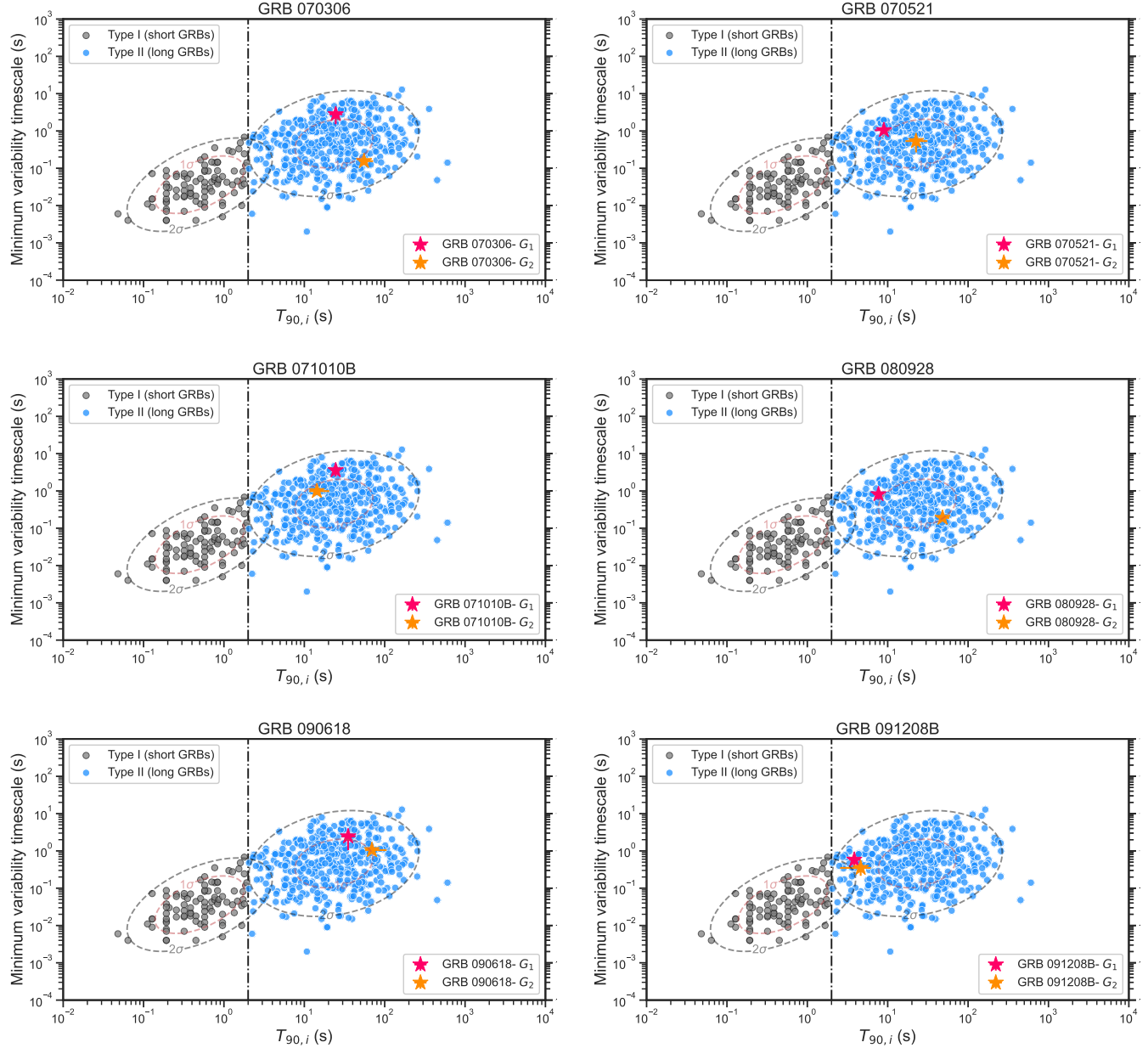
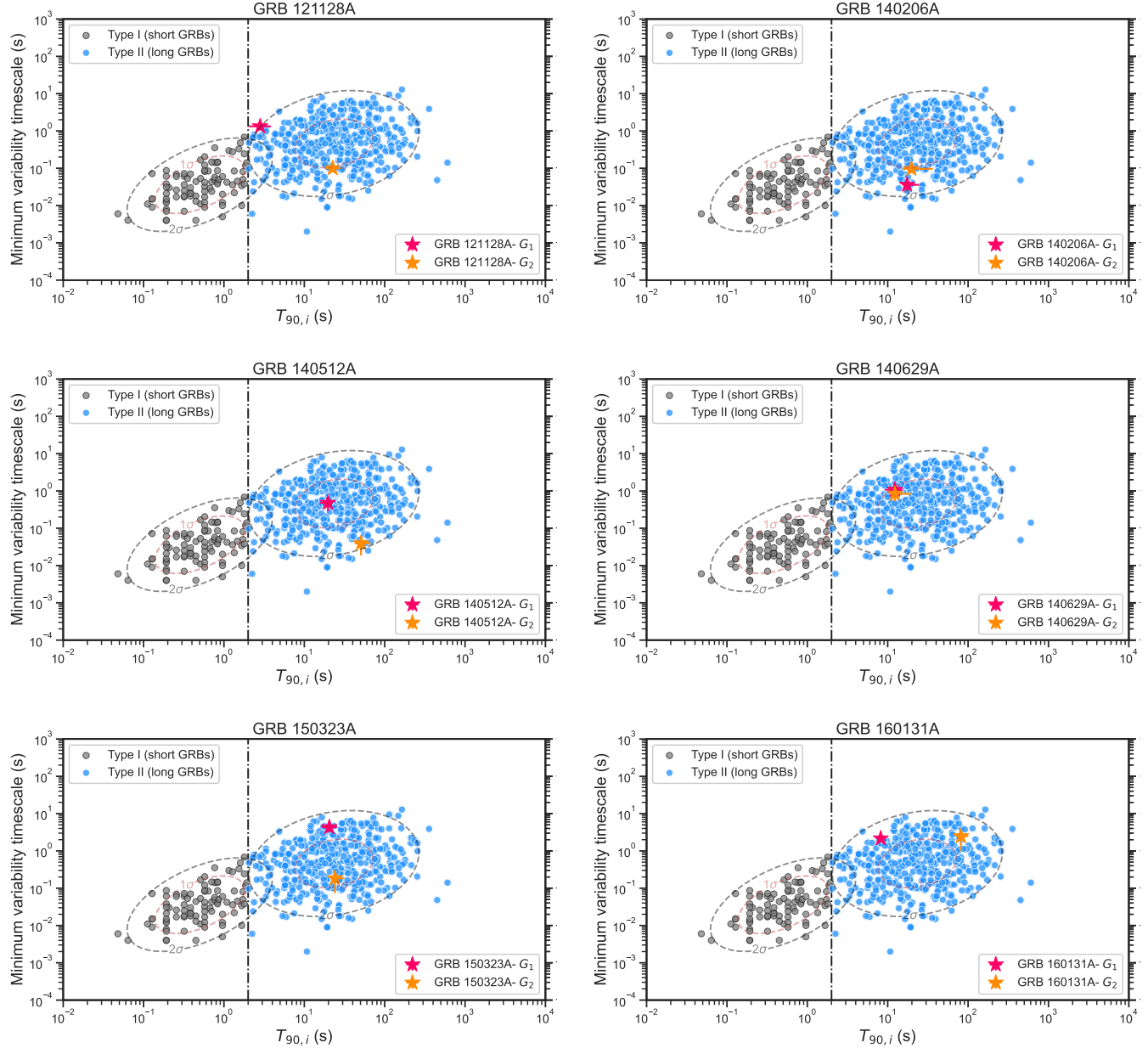


Figure 4. Duration (T_{90}) versus minimum variability timescale (MVT) for precursor (G_1 , red star) and main emission (G_2 , orange star) pulses in the sample. Gray and blue points show the distributions of Type I (short) and Type II (long) GRBs, respectively, from Golkhou et al. (2015). The ellipses represent 1σ clustering regions for each population. While main emissions lie squarely within the Type II region, precursors typically exhibit longer MVTs, indicating smoother temporal structure, yet remain consistent with the collapsar (Type II) population.





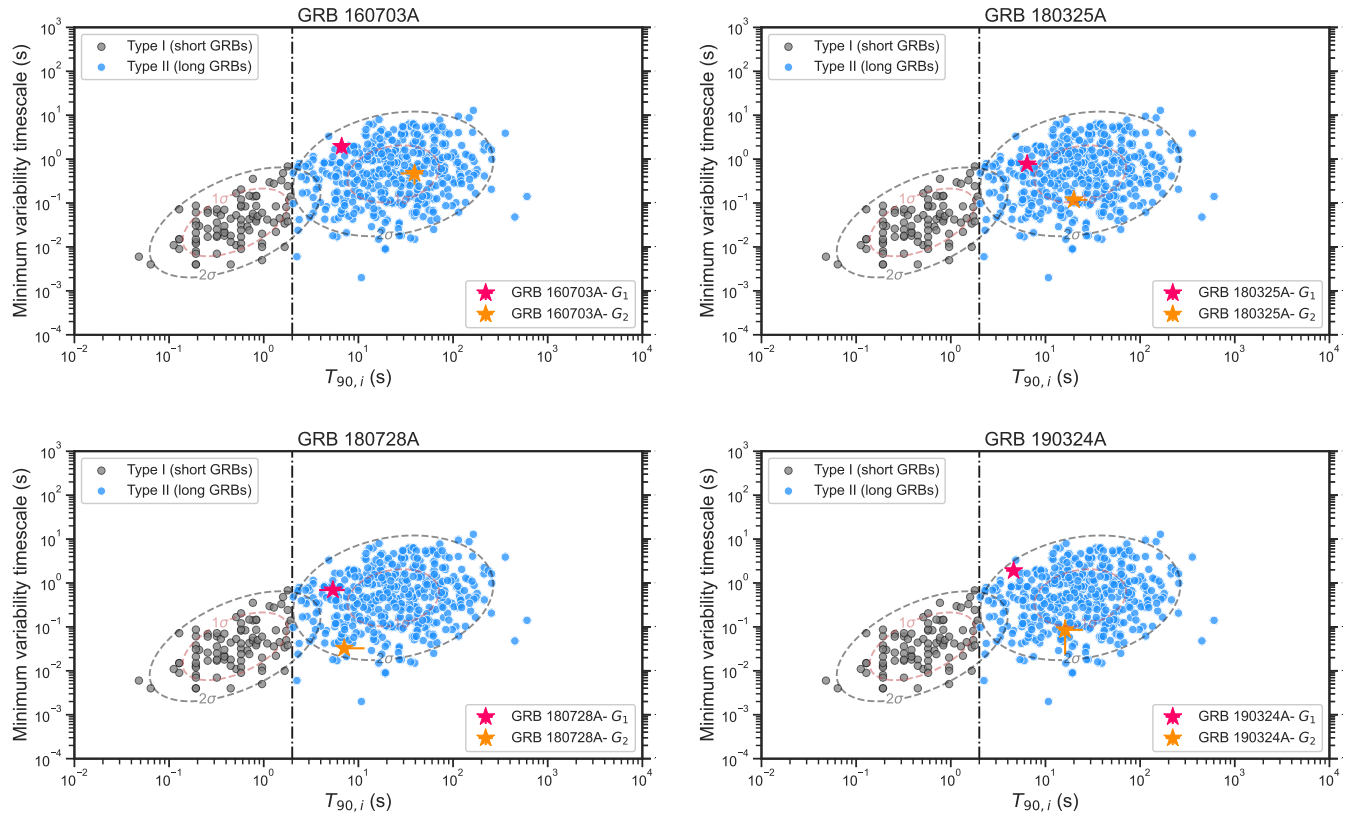


Figure 4— Continued

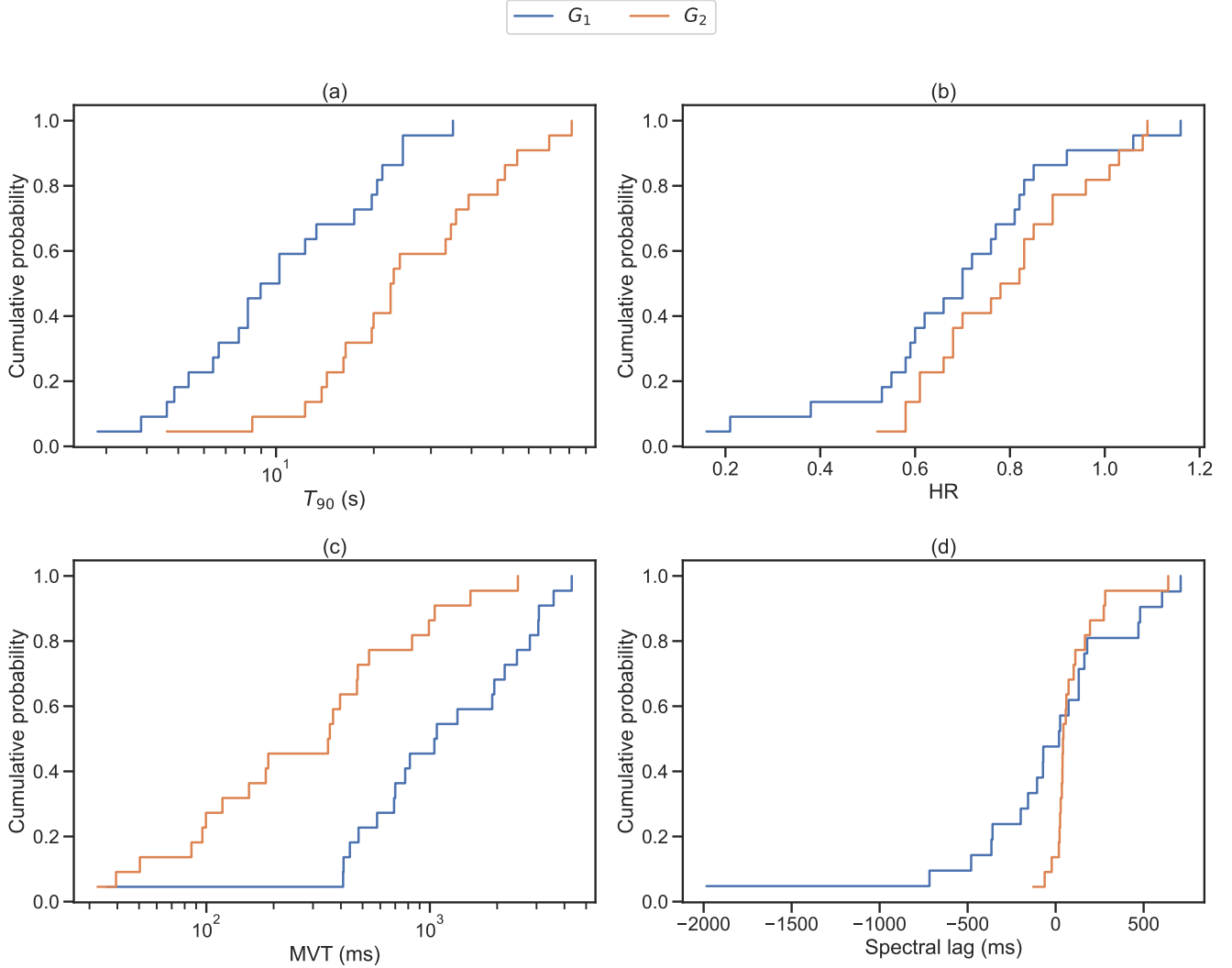


Figure 5. Cumulative distribution functions (CDFs) for episode-level observables in the precursor emission (G_1) and main emission (G_2) phases in our long-duration GRB PE+ME sample. (a), individual T_{90} durations (15–150 keV) of precursor and main burst for each GRB using values from Table 3; (b), hardness ratio (S_{50-100}/S_{25-50}) using values from Table 4; (c), minimum variability timescale (MVT) using values from Table 5; (d), spectral lag between 25–50 and 15–25 keV using values from Table 6. For each parameter, the G_1 and G_2 distributions are plotted separately to highlight systematic contrasts: G_2 episodes are consistently smoother (longer MVT), spectrally softer (lower HR), and exhibit more diverse lags than G_1 .

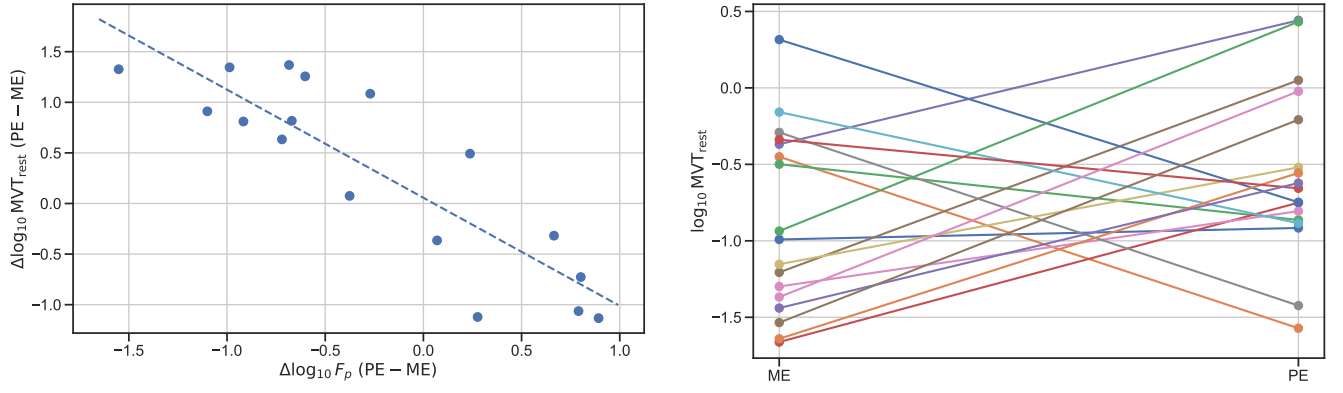


Figure 6. Left-panel: Paired regression: $d\log MVT$ vs $d\log F_p$ (BAT 15–150 keV). Within-burst log-difference of rest-frame minimum variability timescale, $\Delta \log_{10} MVT_{rest}$, versus the log-difference of peak flux, $\Delta \log 10F_p$, for the precursor (PE) relative to the main emission (ME), measured in the same BAT band (15–150 keV). The dashed line shows the OLS fit to the paired data, yielding a significantly negative slope ($\beta = -1.07^{+0.25}_{-0.28}$, $R^2 = 0.75$; Pearson $r = -0.869$, $p = 6.0 \times 10^{-6}$; Spearman $\rho = -0.819$, $p = 5.9 \times 10^{-5}$). The strong anti-correlation demonstrates that weaker (lower-SNR) precursors admit larger measurable MVT, consistent with threshold-driven variability detection. **Right-panel:** Within-GRB paired MVT (rest frame). Paired line plot of $\log_{10} MVT_{rest}$ from the main emission (ME) to the precursor (PE) for each burst. Most trajectories follow the global trend that weaker precursors have larger MVT (consistent with the SNR bias inferred in Figure A), while a minority of events exhibit stronger and more rapidly variable precursors (shorter PE MVT despite higher PE flux), pointing to genuine physical differences in the onset phase (e.g., early internal-shock or magnetically dominated dissipation).